Biophysical Journal
Article

Biophysical Society

G-actin diffusion is insufficient to achieve F-actin assembly in fast-treadmilling protrusions

Ravikanth Appalabhotla,[1] Mitchell T. Butler,[2] James E. Bear,[2,*] and Jason M. Haugh[1,*]
[1]Department of Chemical and Biomolecular Engineering, North Carolina State University, Raleigh, North Carolina and [2]Department of Cell Biology and Physiology, UNC Lineberger Comprehensive Cancer Center, University of North Carolina School of Medicine, Chapel Hill, North Carolina

ABSTRACT To generate forces that drive migration of a eukaryotic cell, arrays of actin filaments (F-actin) are assembled at the cell's leading membrane edge. To maintain cell propulsion and respond to dynamic external cues, actin filaments must be disassembled to regenerate the actin monomers (G-actin), and transport of G-actin from sites of disassembly back to the leading edge completes the treadmilling cycle and limits the flux of F-actin assembly. Whether or not molecular diffusion is sufficient for G-actin transport has been a long-standing topic of debate, in part because the dynamic nature of cell motility and migration hinders the estimation of transport parameters. In this work, we applied an experimental system in which cells adopt an approximately constant and symmetrical shape; they cannot migrate but exhibit fast, steady treadmilling in the thin region protruding from the cell. Using fluorescence recovery after photobleaching, we quantified the relative concentrations and corresponding fluxes of F- and G-actin in this system. In conjunction with mathematical modeling, constrained by measured features of each region of interest, this approach revealed that diffusion alone cannot account for the transport of G-actin to the leading edge. Although G-actin diffusion and vectorial transport might vary with position in the protruding region, good agreement with the fluorescence recovery after photobleaching measurements was achieved by a model with constant G-actin diffusivity $\sim 2\ \mu m^2/s$ and anterograde G-actin velocity less than $1\ \mu m/s$.

SIGNIFICANCE Regulation of the actin cytoskeleton is central to understanding force generation in migrating cells. This process is inherently dynamic, stochastic, and associated with cell shape changes, complexities that hamper estimation of physicochemical parameters such as those characterizing actin monomer transport. To address this, we employed a strategy that compels cells to adopt a steady-state, protruding region; with this experimental system, together with programmed photobleaching and mathematical analysis thereof, we found that monomer transport by diffusion alone (as commonly assumed) cannot explain the data.

INTRODUCTION

In mammalian cells, dynamic polymerization of actin filament networks is critical for cell motility, vesicular trafficking, and the formation of specialized protrusions such as lamellipodia, filopodia, and dendritic spines (1). While much is known about the biochemical and biophysical basis for actin polymerization and depolymerization, several important aspects of this process, such as the recycling of actin monomers from zones of depolymerization to areas of polymerization, are poorly understood. Actin filaments within lamellipodial protrusions constitute a prototypical recycling actin network that has been extensively studied with both experimental and theoretical approaches (2–4), yet there remains a gap between understanding of actin dynamics in reconstituted assays versus intact cells.

In lamellipodial protrusions, actin filament (F-actin) assembly and disassembly tend to be spatially separated, with monomer (G-actin) incorporation largely occurring at the leading membrane edge and disassembly occurring some distance away. F-actin polymerization occurs on free barbed ends of filaments and is facilitated by both actin polymerases, such as Ena/VASP proteins and formins, as well as by *de novo* nucleation via activation of the Arp2/3 complex (5). Disassembly of actin networks is driven by ADF/cofilin proteins that sever filaments and enhance

Submitted April 1, 2023, and accepted for publication August 25, 2023.
*Correspondence: jbear@email.unc.edu or jason_haugh@ncsu.edu
Ravikanth Appalabhotla and Mitchell T. Butler contributed equally to this work.
Editor: Alex Mogilner.
https://doi.org/10.1016/j.bpj.2023.08.022

depolymerization (6). In addition, actin filament breakage by the force of nonmuscle myosin II (NMII) contributes to filament disassembly (7). These assembly and disassembly reactions have been studied intensively, to the extent that a quantitative understanding has been established (2,3). In solution, with well-mixed components, it is readily determined how rates of F-actin assembly/disassembly are related to G-actin concentration. In actively migrating cells, however, those relationships are difficult to characterize, in part because 1) "working" filaments acting to push the membrane forward are subject to force-dependent feedbacks (3,8–10) and 2) such regions stochastically advance and retract. How actin monomers relocate from the rear to the front of the actin network to complete the "treadmilling" cycle in lamellipodia is incompletely understood.

Two mechanisms have been considered for actin monomer recycling to the front of the network at the leading edge: diffusion and some form of vectorial transport. Several experimental and theoretical studies have concluded that diffusion alone is sufficient to account for actin monomer movement from the zone of depolymerization to the front of the network for repolymerization (11,12). Others have concluded that advective fluid flow and active, motor-driven transport also contribute. The bulk flow hypothesis postulates that contraction and disassembly of the actin network by NMII produces an osmotic pressure gradient that manifests as an advective flow from rear to front (13). Other work suggests that the unconventional myosin motor, Myo1c, may be responsible for actin monomer anterograde transport (14). Despite such attempts to characterize G-actin transport from the site(s) of depolymerization back to the leading edge, the question of whether or not G-actin diffusion is sufficient to account for the flux of F-actin assembly remains unclear.

A significant barrier to resolving this question is the difficulty of comparing results from disparate cellular contexts. In particular, some lamellipodia are dynamic, displaying cycles of protrusion and retraction that alter cell shape. The complexity of leading-edge morphodynamics is inherently interesting, but it confounds analysis of actin dynamics in terms of local rates of actin polymerization and depolymerization. In addition, as lamellipodia engage the substrate over which they protrude, adhesion receptors such as integrins form attachments to adhesive, extracellular matrix-associated ligands such as fibronectin (Fn), which are naturally found in the extracellular matrix during fibroblast invasion of wounded tissue (15). The adhesive bonds mediate both physical actin network clutching (facilitating protrusion) and activation of signaling pathways that tune actin polymerization/depolymerization kinetics.

To analyze the flux of G-actin incorporated into filaments at the leading edge, an ideal experimental system would show negligible shape change over time, while supporting rapid and persistent actin polymerization and depolymerization (treadmilling); this scenario dramatically simplifies mathematical modeling of the actin dynamics. To achieve this, we reasoned that F-actin polymerization ought to be unfettered by adhesive interactions with the underlying substrate. Here, we introduce just such a model system. Analyses of fluorescence recovery after photobleaching (FRAP) experiments were designed, in conjunction with modeling predictions, to more accurately define the mode(s) of actin monomer transport to the cell periphery.

MATERIALS AND METHODS

Fn surface patterning

Single-cell micropatterning was performed essentially as described (16), with minor modifications. Microscope cover glasses (Marienfeld Superior 25 mm, No. 1.5H; Paul Marienfeld GmbH & Co. KG, Germany) were cleaned with 70% ethanol and dried with an air hose before plasma cleaning for 90 s (high power with PDC-32G Basic Plasma Cleaner; Harrick Plasma, Ithaca, NY). After plasma cleaning, cover glasses were incubated with a 0.1 mg/mL solution of PLL-g-PEG (SuSoS AG, Dübendorf, Switzerland) in 15 mM HEPES (pH 7.4) for at least 30 min up to overnight at room temperature. Cover glasses were then rinsed with water and dried shortly before surface patterning.

Surface patterning was achieved using a chrome photomask on a quartz substrate (Photo Sciences, Torrance, CA) with arrays of square and triangle microfeatures (30 μm edges) and circles (30 μm diameter). The patterned shapes allow deep UV light to locally irradiate and desorb the PLL-g-PEG coating in discrete shapes and regions, amenable to subsequent Fn coating and cell attachment.

The chrome side of the photomask was first illuminated with deep UV for 3 min (UVO-Cleaner, Model 24; Jelight, Irvine, CA), and then 5 μL of water was added on the chrome side over the desired photopatterning region as a buffer before gently pressing down the PLL-g-PEG-coated cover glass against the photomask, oriented with the PLL-g-PEG-coated side down against the photomask. The photomask with the attached cover glass(es) was then illuminated again with deep UV, this time inverting the photomask so that the light passed through the quartz side first to the chrome side with the cover glass affixed below. After this second illumination, the chrome side of the mask was flooded with water to allow the gentle detachment and flow of the cover glass(es) to the edge of the mask for careful retrieval with plastic forceps. After another gentle wash with water, the cover glasses were secured in imaging chambers (Attofluor A-7816; Thermo Scientific, Waltham, MA) and coated with a solution of 20 μg/mL human Fn (Corning, Corning, NY) in PBS for 20 min at room temperature. A final wash with PBS was performed before adding cells and imaging.

Live-cell imaging

Cells used for capturing live cell micrographs of actin dynamics are from a diploid clonal population of mouse dermal fibroblasts (JR20) that were stably expressing GFP-β-actin via lentiviral transduction, and were cultured and imaged in high glucose DMEM (Gibco; Thermo Scientific, Waltham, MA) supplemented with 10% FBS (MedSupply Partners, Atlanta, GA) and GlutaMAX (Gibco) at 37°C with 5% CO_2. JR20s were lifted from culture dishes using 0.25% Trypsin-EDTA (Gibco), and approximately 22,500 cells were seeded in imaging chambers with surface-patterned cover glasses. After allowing the cells to settle onto the Fn patterns for 30 min, the imaging/culture medium was gently pipetted up and down and replaced with fresh medium to remove a portion of the unattached cells.

Images were captured starting 45 min after seeding cells with a Zeiss LSM800 confocal microscope using a Plan-Apochromat 63×/1.4 NA oil objective with a 1.7 μm optical section. Images were collected at 512 × 512 pixels with 16 bits per pixel, typically using 0.2% laser power of a 10 mW, 488 nm laser. For closely monitoring individual protrusions, 22.5 × 22.5 μm regions with a 0.04 μm pixel size were collected, while

whole-cell time lapse movies typically encompassed a 67.6 × 67.6 μm region with a 0.13 μm pixel size. For the visualization of actin polymerization and retrograde flow rates, discrete regions near the edge of protrusions were bleached (100% power of 10 mW 488 laser, 1.03 μs pixel dwell time, 4 iterations) and subsequently monitored at approximately 1 s per frame, with additional bleaches occurring every 60 frames. For cytochalasin D (CytoD) wash-in experiments, time lapse movies were paused for roughly 20 s for the addition of 200 μL of 5 μM CytoD to the 800 μL of cells and medium already present in the imaging dish (giving a 1 μM working concentration). Bleaching of post-CytoD leading-edge actin was performed with similar settings as above.

Image quantification and presentation

The Fiji distribution of ImageJ was used to extract and measure the relevant metrics from live-cell imaging data. For the measurement of retrograde flow rates, kymographs were generated from 5-pixel-wide line scans over regions of leading cell edges labeled with GFP-actin during sequential bleaching every 60 frames (~1.0 s per frame). The slope of the line from the leading edge of the protrusion to the interface between bleached and unbleached actin incorporated into the filamentous actin network after the bleach could be easily visualized in these kymographs and used to accurately calculate retrograde flow rates at an approximately steady state. For the measurements of leading-edge GFP-actin intensity shown in Fig. 2, an approximately 10 μm long (along the periphery of the spillover) and 1 μm wide (from the edge toward/into the cell body) region of interest was manually drawn for intensity measurements in this region.

Raw single-plane images were copied from Fiji, and the Despeckle and Gaussian Blur (radius: 0.5 pixels) filters were applied in Photoshop (Adobe). Multiplane image stacks were viewed as 3D reconstructions in Imaris (Oxford Instruments, Abingdon, Oxfordshire, UK). Figures were assembled, arranged, and labeled in Illustrator (Adobe), and graphs were generated with Prism (GraphPad, San Diego, CA). Prism was also used to fit one-phase exponential curves to leading edge GFP-actin FRAP data after CytoD treatment, yielding estimated plateau and half-life values. Recovery curves that could not be fit with a one-phase exponential curve were disregarded as outliers (2 out of 17 cells assessed).

For full-span FRAP experiments that were compared with simulation predictions (Figs. 3 and 5), MATLAB (The MathWorks, Natick, MA) was used for image processing. Image stacks were background subtracted, segmented, and cropped. Crop dimensions were determined by first using the bleach region of interest coordinates (extracted from the image metadata) to identify the position of interest, and the crop width was set by subtracting ~0.5 μm from each of the left and right edges. The crop length was set to include both the leading and adhesive edges. For each cropped image matrix in the time series, the intensity values were smoothed with a moving average smoothing filter applied across the length of the image (traversing the spillover protrusion from the leading edge to the adhesive edge). Then, for each column (y value) of each image matrix, the leading-edge position was estimated as the maximum value in the column, and positions x were aligned relative to that pixel. Pixel intensities for each column were normalized by the mean of the prebleach intensities of the leading-edge pixel and its 10 nearest neighbors (spanning ~0.5 μm), averaged also temporally over the 5 images just before bleaching. Finally, a single fluorescence profile for each image was obtained by averaging across the aligned, normalized columns.

Model of actin transport at steady state

Here, we examine a domain corresponding to the nonadhesive region, with spatial coordinate x (μm) measured from the leading edge and spatial coordinate y parallel to the leading edge; the z dimension, measured across the height of the domain, is considered thin, and so all concentrations are considered averages over the height. As with other continuum models of actin dynamics, and consistent with the analysis of fluorescence image data, F- and G-actin are homogenized into a single, fluid medium/phase. The basic model assumption is that the system is at (quasi-) steady state. The reader is referred to Text S1, section 1, in which we derive the general steady-state relationships, with full consideration of all states of G-, F-, and membrane-bound actin, and of direct versus polymerase-mediated F-actin elongation.

To model the steady-state conservation of F-actin (concentration F) and of G-actin (concentration G) at any point within the nonadhesive region, the y dimension may be considered semi-infinite, and so the steady-state problem is one-dimensional (1D). For F-actin, net retrograde transport is balanced by net disassembly, considering local rates of depolymerization, r_{depol}, and polymerization, r_{pol}. The forms of these rate terms will be specified, but for now we show what general results may be derived.

$$\frac{\partial F}{\partial t} = -\frac{\partial N_F}{\partial x} - r_{depol} + r_{pol} = 0$$

$$N_F = V_F F$$

$N_F(x)$ is the flux of F-actin, and $V_F(x)$ is the retrograde flow velocity (which points in the positive x-direction). For G-actin,

$$\frac{\partial G}{\partial t} = -\frac{\partial N_G}{\partial x} + r_{depol} - r_{pol} = 0$$

$N_G(x)$ is the flux of F-actin. With conservation of total actin in 1D, we obtain flux matching conditions.

$$N_F|_{x=0} = -N_G|_{x=0} = N_{pol}$$

$$N_F(x) = -N_G(x) = N(x)$$

Except where noted otherwise, we assume that all states of G-actin have the same transport parameters, with

$$N_G = -D_G\frac{dG}{dx} - V_G G$$

$D_G(x)$ is the effective diffusivity of G-actin in the domain, and $V_G(x)$ is the anterograde velocity (which points in the negative x-direction); both are potentially position dependent.

To proceed further, we need to assume the forms of $V_F(x)$, $r_{depol}(x)$, $r_{pol}(x)$, $D_G(x)$, and $V_G(x)$. Supported by empirical measurements for this system, we take

$$V_F(x) \approx \text{constant}$$

And, consistent with previous modeling work (17–20), we considered first-order turnover of F-actin,

$$r_{depol}(x) = k_{depol}F(x)$$

After photobleaching, we do not observe structured recovery of fluorescence throughout the bleached region, and therefore for our system we take

$$r_{pol} \approx 0$$

With these specifications, and the boundary condition $F(0) = F_0$

$$F(x) = F_0 \exp\left(-\frac{k_{depol}}{V_F}x\right)$$

$$N(x) = D_G\frac{dG}{dx} + V_G G = V_F F$$

As for the G-actin transport parameters, we considered two distinct cases. In the first, we assume that D_G and V_G are constants, with values $D_{G(c)}$ and $V_{G(c)}$, respectively. With the boundary condition $G(0) = G_0$, the solution in this case is

$$G(x) = \alpha F_0 \exp\left(-\frac{k_{depol}}{V_F}x\right) + (G_0 - \alpha F_0)\exp\left(-\frac{V_{G(c)}}{D_{G(c)}}x\right);$$

$$\alpha = \frac{V_F}{V_{G(c)} - D_{G(c)}\dfrac{k_{depol}}{V_F}}$$

In the limit of $V_{G(c)} = 0$, the equation above reduces to

$$G(x) = G_0 + \frac{{V_F}^2 F_0}{k_{depol} D_{G(c)}}\left[1 - \exp\left(-\frac{k_{depol}}{V_F}x\right)\right]$$

An even more specific limit, referred to as diffusion-only, diffusion-limited (DODL) takes the above equation with $G_0 = 0$ and names $D_{G(c)}$ as $D_{G,DODL(c)}$.

The second case we examined was DODL but with nonconstant diffusivity, $D_{G,DODL}(x)$. With the assumption that $D_{G,DODL}(x)$ is a smoothly increasing or decreasing function (G-actin diffusion is slower or faster as molecules approach the leading edge),

$$D_{G,DODL}(x) = D_{G,0} + (D_{G,\infty} - D_{G,0})\left(1 - e^{-x/\lambda L}\right)$$

Here, $D_{G,0}$ and $D_{G,\infty}$ are the values of $D_{G,DODL}(x)$ at and far from the leading edge, respectively, L is the measured span of the nonadhesive region, and dimensionless λ characterizes the slope of the function. In the analyses performed, $\lambda = 0.3$ was used.

Model parameterization from experimental inputs

The F-actin retrograde flow velocity, V_F, was estimated from the experimental kymograph as described above. Background-subtracted fluorescence intensities were expressed as a fraction of the total GFP-actin intensity at the leading edge, prebleach. Accordingly, in the model, normalized concentrations are

$$f(x) = \frac{F(x)}{F_0 + G_0}; \quad g(x) = \frac{G(x)}{F_0 + G_0}$$

To determine sets of model parameter values consistent with a particular FRAP experiment, the normalized pre- and postbleach fluorescence intensities were quantified some distance x_{match} from the leading edge (close to the interface between the nonadhesive and adhesive zones). The postbleach intensity was measured a short time (~5–10 s) after bleaching such that the G-actin fluorescence had stabilized. Thus, $f(x_{match})$ and $g(x_{match})$ were estimated. Based on the estimated values of V_F and $f(x_{match})$, the value of k_{depol} was estimated. The value of $D_{G,DODL(c)}$ was estimated as follows.

$$D_{G,DODL(c)} = \frac{V_F L}{g(x_{match})}\left[\frac{1 - f(x_{match})}{-\ln f(x_{match})}\right]$$

To identify combinations of $D_{G(c)}$, $V_{G(c)}$, and g_0 as scenarios consistent with estimable quantities, values of $D_{G(c)}$ and g_0 were assumed, and the value of $V_{G(c)}$ was determined by matching the estimated value of $g(x_{match})$. For the case of nonconstant $D_{G,DODL}(x)$, the value of $D_{G,0}$ was assumed, and the value of $D_{G,\infty}$ was determined by matching the estimated value of $g(x_{match})$.

FRAP predictions

We refer to $f_{un}(x,y,t)$ and $g_{un}(x,y,t)$ as the normalized concentrations of unbleached (fluorescent) F-actin and G-actin, respectively. They are initialized according to the steady-state $f(x)$ and $g(x)$ profiles established in the previous sections. Contained within the domain, there is a defined region in which bleaching occurs with first-order rate constant $k_{bleach}(x,y,t)$; its time dependence reflects that bleaching is turned on and off at specified times. The conservation equation and boundary condition for f_{un} are

$$\frac{\partial f_{un}}{\partial t} = -k_{bleach} f_{un} - V_F\frac{\partial f_{un}}{\partial x} - k_{depol} f_{un};$$

$$f_{un}(0,y,t) = \left[\frac{f(0)}{g(0)}\right] g_{un}(0,y,t)$$

The boundary condition effectively assumes that actin polymerization at the leading edge is in pseudoequilibrium with the local G-actin concentration; this is to say that all G-actin at the leading edge is equally polymerizable, and that the lifetimes of G-actin interactions with polymerases, mediated by profilin, are short. The latter assumption is readily justified, considering that measured off-rates of profilin-mediated interactions are quite fast (21,22), and measured elongation rates for the processive polymerases are ~10–1000 monomers/s (8,23) (further analysis provided in Text S1, section 2). The singularity introduced when $g(0) = 0$ is avoided by using a small but nonzero value. For g_{un},

$$\frac{\partial g_{un}}{\partial t} = -k_{bleach} g_{un} + \nabla\cdot(D_G \nabla g_{un}) + V_G\frac{\partial g_{un}}{\partial x} + k_{depol} f_{un};$$

$$\left(D_G\frac{\partial g_{un}}{\partial x} + V_G g_{un}\right)\Big|_{x=0} = V_F\left[\frac{f(0)}{g(0)}\right] g_{un}(0,y,t);$$

$$g_{un}(L,y,t) = g(L);$$

$$\frac{\partial g_{un}}{\partial y}\Big|_{y=0} = \frac{\partial g_{un}}{\partial y}\Big|_{y=W} = 0$$

The boundary condition at $x = L$, the interface between nonadhesive and adhesive regions, assumes a constant value, calculated from the prebleach steady state equation for $g(x)$. The justification for this is that the rear of the bleach zone backs up to the bulk of the cell volume and to a concentrated depot of disassembling F-actin. This assumption is critically assessed through ancillary simulations (Text S1, section 3 and Fig. S1).

Models with two G-actin species

In the models described above, states of G-actin are lumped together with respect to both transport properties and leading-edge polymerizability. To address the possibilities of diffusion-only scenarios with those assumptions relaxed, we formulated models with two G-actin species. The steady-state and FRAP equations for these models are presented and analyzed in Text S1, sections 4 and 5.

Model implementation

FRAP protocols were simulated by solving the partial differential equations in the VCell software environment (24), with the fully implicit finite volume (variable time step) solver. Not shown in the conservation equation for f_{un} is a very slow diffusion term, added to promote numerical stability ($D_F = 1 \times 10^{-5}$ $\mu m^2/s$), along with the arbitrary boundary condition, $f_{un}(L,y,t) = f(L)$. For preliminary, 1D simulations, the length of the spillover region was 10 μm, and the full-bleach FRAP protocol was simulated with a bleaching rate constant of 200 s^{-1} and a duration of 0.1 s, comparable with experiments. For 2D simulations matched to experiments, the rectangular geometry was 20 μm wide, and the length was chosen to match the span of the particular nonadhesive region. The bleached region and bleach duration were parameterized to match the experimental bleaching protocol of each experiment, and the simulation results were analyzed in the same fashion as the experiment. To mitigate "numerical diffusion," which arises when transport of some species is dominated by advection (25), fine meshes were employed, and control simulations confirmed that the contribution of numerical diffusion was acceptably low. For 1D simulations, we used a mesh size of $\Delta x = 5 \times 10^{-5}$ μm and a maximum time step of 0.1 s. For 2D simulations, we elected to mesh the geometry with $\Delta x \leq 0.0028$ μm and $\Delta y = 0.1$ μm, which was sufficient to ensure a second-order accurate discretization for G-actin in our cohort of simulations. The primary simulations may be accessed in VCell under user name, ra_mb_jb_jmh.

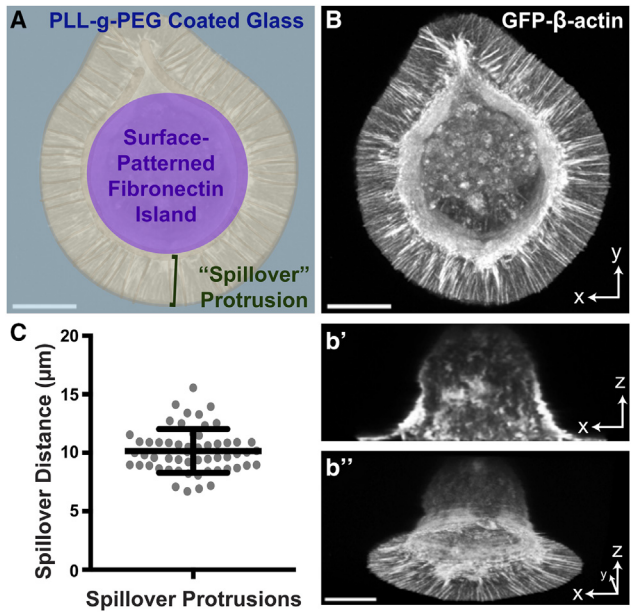

FIGURE 1 Fibroblasts extend flat, roughly uniform, and steady-state protrusions over PLL-g-PEG from surface-patterned Fn attachment sites. (*A*) Schematic of cell-plating conditions for the analysis of actin dynamics in steady-state "spillover" protrusions over PLL-g-PEG-coated glass surfaces from surface patterned Fn attachment sites. (*B*) GFP-actin stably expressed in JR20 cells (mouse dermal fibroblasts) that has been plated as schematized in (*A*) was visualized and captured in a series of images along the Z-plane, displayed as a maximum intensity projection. A cross section from the Z-stack projected in (*B*) is shown in (*b'*), and a pseudo side view of a 3D reconstruction is shown in (*b"*). Scale bars, 10 μm. (*C*) Graph of the approximate average cell protrusion distance outward from the edge of micropatterned Fn shapes in JR20s stably expressing GFP-actin. Bars represent the mean ± standard deviation ($n = 56$ protrusions from 3 independent experiments). To see this figure in color, go online.

RESULTS

A simplified system to interrogate actin dynamics in protrusions

To examine the dynamics of G-actin diffusion and F-actin retrograde flow in cell protrusions that adopt reproducible shapes, we used surface micropatterning of Fn islands on microscope cover glasses that are surrounded by nonadhesive PLL-g-PEG. A variety of shapes were tested, including squares with 30 μm edges, triangles with 30 μm edges, and circles with 30 μm diameters. On shapes of this size, JR20 mouse dermal fibroblasts (26) attach to and fill the Fn patterns. Interestingly, these cells make protrusions of a relatively uniform radial length that "spill over" the edge of the original pattern (Fig. 1 *A*). These spillover protrusions are flat, with a nearly uniform thickness, and they are filled with a mixture of bundled F-actin microspikes and actin filament mesh as visualized by expression of GFP-actin (Fig. 1 *B*). Measurements of the spillover protrusion distance from the adhesive boundary show an average of about 10 μm, with a standard deviation of less than 2 μm (Fig. 1 *C*). Thus, spillover protrusions are highly consistent from cell to cell despite apparent heterogeneity in the cell population when plated on evenly coated Fn substrates. This provides us with large, relatively uniform regions to monitor actin polymerization and recycling dynamics.

Monitoring spillover protrusions over time show that they are quite stable, with very little fluctuation in protrusion distance and infrequent retraction events (Fig. 2 *A*). To assess various dynamic behaviors of GFP-actin, we bleached different regions of the spillover protrusions, either at discrete regions behind the leading edge or sections that span the full distance of the spillover, from the leading edge to the outer boundary of the Fn attachment site (Fig. 2 *A*; Videos S1 and S2). This allows for the visualization and measurement of the retrograde flow rates of the treadmilling actin network, which, under these circumstances, averages 11.4 μm/min (Fig. 2 *B*). This actin polymerization rate is considerably faster than the 3.6 μm/min observed when this cell line is plated on evenly coated 10 μg/mL Fn-coated glass (26), suggesting that there is significantly less resistance to the retrograde flow here, or clutching, and that the polymerization rate may be nearing the maximum rate for these cells. An additional, telling feature of these bleaching experiments is the almost immediate appearance of a thin, dark band in the F-actin network. This band is both preceded and followed by unbleached actin populations (Fig. 2 *A*, *red arrows*), indicating that bleached G-actin is rapidly incorporated in F-actin arrays at the leading edge.

In addition to bleaching discrete regions of spillover protrusions, we also bleached all the GFP-actin either contained in the spillover protrusion or in the cell body above the patterned Fn adhesive zone (Fig. 2 *C*; Videos S3 and S4). Monitoring the intensity of GFP-actin along the furthest edge of the spillover

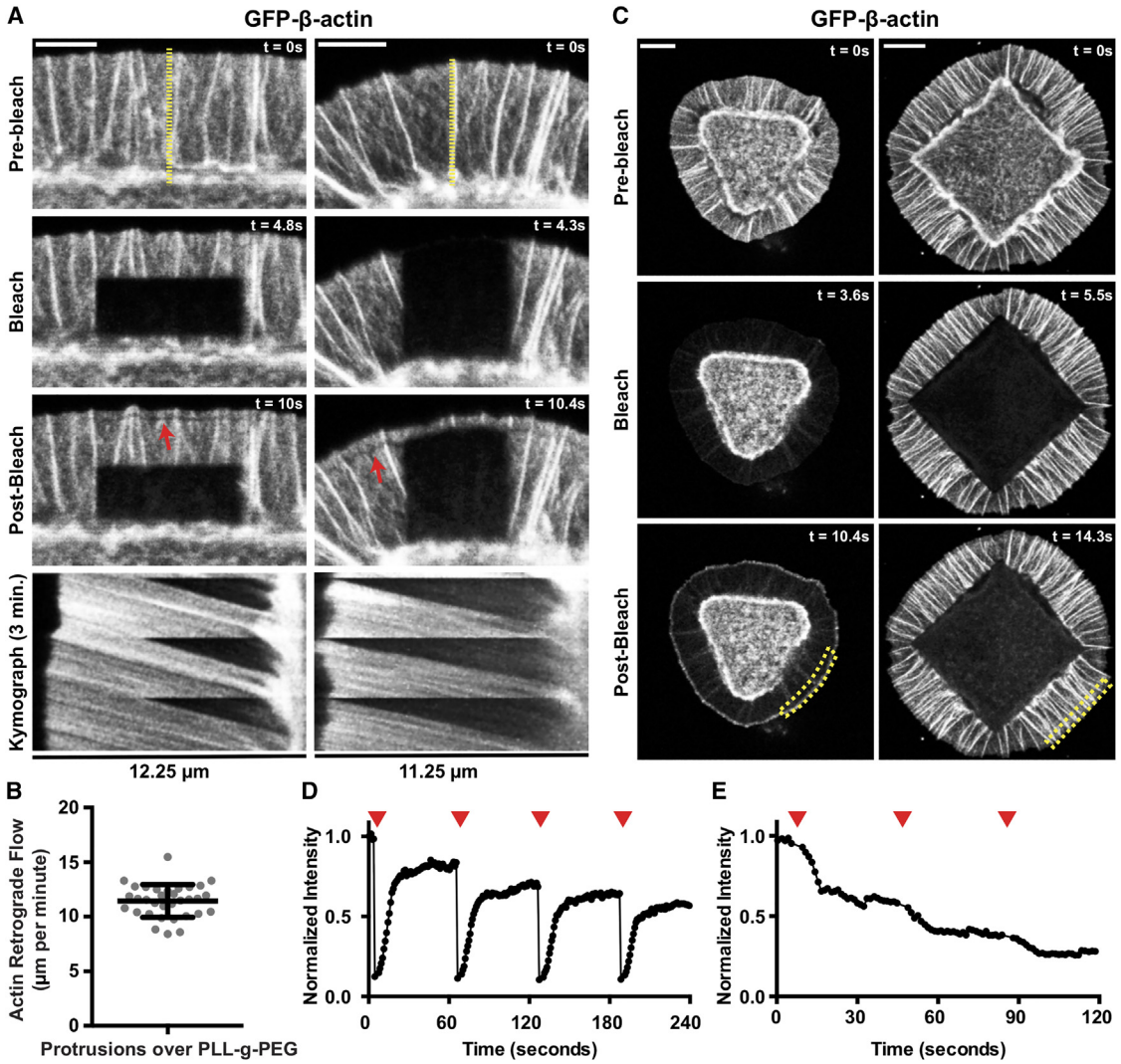

FIGURE 2 Bleached and unbleached GFP-actin are incorporated into F-actin structures at the leading edge of spillover protrusions. (*A*) Still images and associated kymographs from a time lapse series of micrographs of JR20s expressing GFP-actin that were plated as detailed in Fig. 1 *A*, focused on regions between the edge of a Fn attachment site and the edge of a cell protrusion as different regions of the protrusion are photobleached. Yellow lines show the regions the kymographs below were generated from, and red arrows signify where GFP-actin was bleached and then incorporated into the treadmilling actin filaments at the leading edge. Scale bars, 5 μm. (*B*) Graph of the retrograde flow rate of GFP-actin in spillover protrusions measured from kymographs like those shown in (*A*). Bars represent the mean $\pm$ standard deviation ($n = 33$ protrusions from 3 independent experiments). (*C*) Still images from a time lapse series of micrographs of JR20s expressing GFP-actin that were plated as detailed in Fig. 1 *A* and bleached throughout the entire protrusive area (*left column*) or cell body over the Fn attachment site (*right column*) every 60 frames. Yellow regions indicate areas measured for intensity traces shown in (*D* and *E*). Scale bar, 10 μm. (*D*) Trace of the normalized GFP-actin intensity over time in the region indicated by the yellow dotted outline in the bottom-left panel of (*C*). Red arrows mark photobleaching events of the entire protrusive spillover region of the cell. (*E*) Trace of the normalized GFP-actin intensity over time in the region indicated by the yellow dotted outline in the bottom-right panel of (*C*). Red arrows mark photobleaching events of the entire region of the cell that sits over the square Fn attachment cell-adhesive pattern. To see this figure in color, go online.

protrusion over time while repeatedly bleaching either the spillover or adhesive zone show that there is strong recovery when the spillover is bleached, with a loss of roughly 10–15% of the maximum intensity per each bleaching event (Fig. 2 *D*). However, when the cell body over the adhesive zone is bleached instead, there is a continuous, dramatic decrease in intensity at the periphery of the spillover protrusion, with the mean intensity trending downward after each bleach and shallowing out around a 30–40% loss with each bleach (Fig. 2 *E*). Thus, it appears as if most of the actin being incorporated into the F-actin network of the spillover protrusion at any given time originates from the cell body rather than the spillover being a more self-contained structure with significant local recycling. This characterization is similar to what has been reported for cells plated under more standard conditions (12), but quite different from characteristics ascribed to other cellular contexts for which local actin polymerization is considered substantial (27,28).

Experimental inputs constrain a model of steady-state actin dynamics and FRAP predictions

The representative kymographs shown in Fig. 2 *A* and the associated movies show several consistent and telling features of our system.

1) Averaging out the small fluctuations, the polymerization and depolymerization of F-actin in the protrusion are approximately at steady state.
2) Retrograde flow of F-actin exhibits constant velocity across the nonadhesive region.
3) FRAP near the back end of the bleached area approaches a plateau within ∼5 s, to a fluorescence intensity that is much lower than the prebleach intensity and lacking discernible structure/texture. We therefore attribute this early recovery to the restoration of unbleached G-actin into the region, with no evidence of local actin polymerization.
4) The F-actin structures in the nonadhesive region exhibit variable but consistently modest decreases in intensity (depolymerization) as they flow from the leading edge. Once they arrive at the interface with the adhesive region, the F-actin is compacted in a dense structure, where most of its disassembly must occur.

For each of seven cells that were photobleached in a consistent manner, with the bleached region spanning the spillover protrusion (Fig. 3 *A*), we estimated four quantities: the span of the nonadhesive region, L; the constant velocity of F-actin retrograde flow, V_F; and the intensities attributable to G- and F-actin at a distance x_{match} from the leading edge, close to the back of the bleached region ($g(x_{match})$ and $f(x_{match})$, respectively), normalized by the prebleach intensity at the leading edge (Fig. 3 *B*). Among the cells in the cohort, the estimated values of those quantities are reasonably consistent (Fig. 3 *C*).

The four experimental inputs constrain the parameterization of a basic mathematical model of actin dynamics at steady state (materials and methods and Fig. 4 *A*), as manifest prebleach. The steady-state nature of the system permits dramatic simplification of the model, such that most molecular details related to actin regulation do not need to be specified or assumed (materials and methods and Text S1). With just one other key assumption—that all G-actin at the leading edge is equally polymerizable—any set of G-actin transport parameters that matches the measurable constraints yields a prediction of the dynamics observed during any FRAP protocol, which can be compared with the corresponding experiment. Principally, we sought to determine

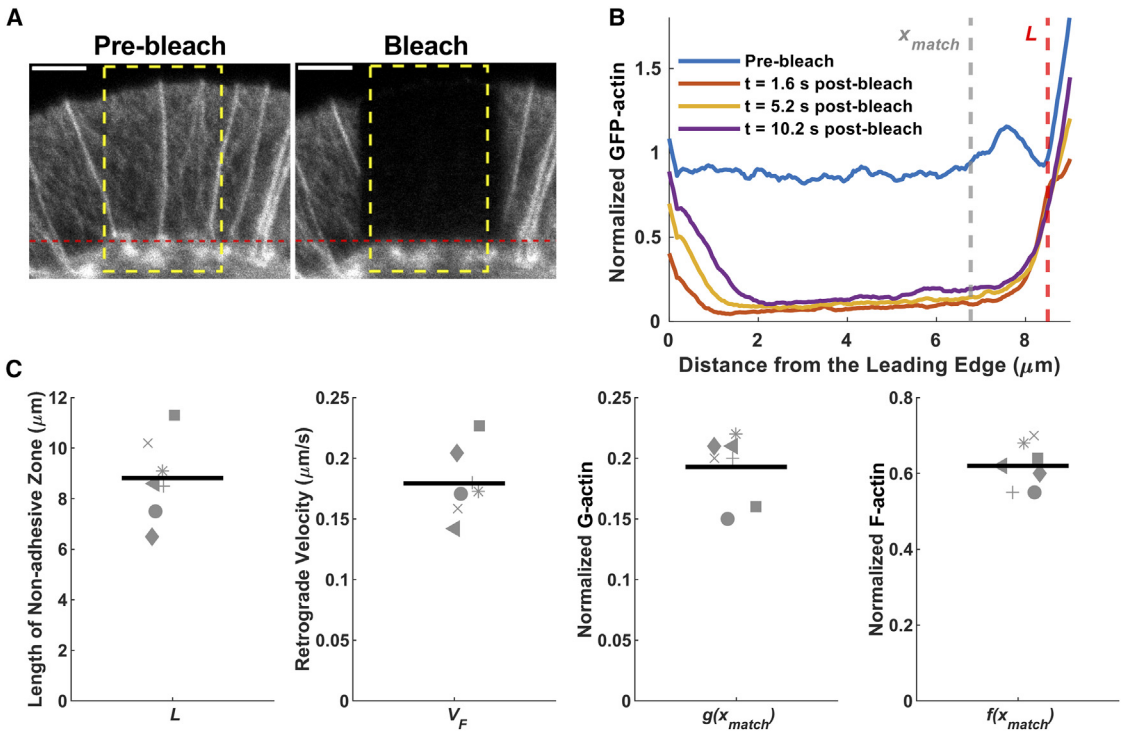

FIGURE 3 Experimental inputs that constrain parameterization of quantitative models. (*A*) For a cohort of seven cells, the full span of the nonadhesive region was rapidly bleached. For each cell, the span of region L was estimated from the prebleach image (*red dashed lines*). The spatial profiles of GFP-actin fluorescence pre- and postbleach were averaged across most of the width of the bleached area (*yellow dashed rectangle*). F-Actin retrograde flow velocity, V_F, was estimated from the associated kymograph. Scale bar, 3 μm. (*B*) Plot of the spatial profiles of GFP-actin fluorescence pre- and postbleach. At a suitable distance from the leading edge, $x = x_{match}$, the normalized, prebleach fluorescence was attributed to the sum of F- and G-actin [$f(x_{match}) + g(x_{match})$], whereas the normalized fluorescence ∼5 s postbleach was attributed to G-actin [$g(x_{match})$]. (*C*) The four experimental estimates for each cell in the cohort (each with a unique symbol) are plotted. To see this figure in color, go online.

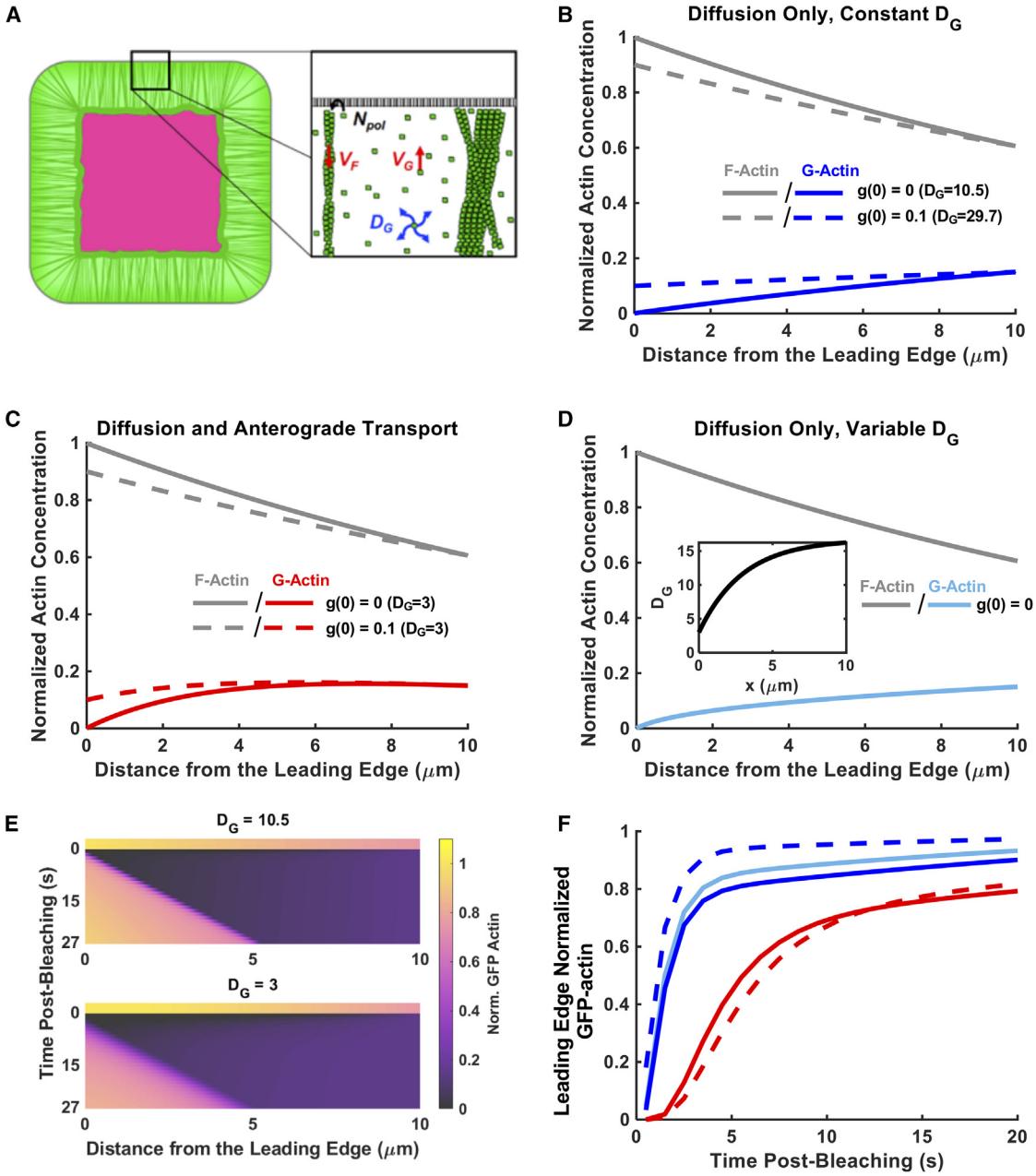

FIGURE 4 Model predictions of FRAP experiments demonstrate that G-actin transport to the leading edge by diffusion only is distinguishable from transport aided by anterograde drift. (*A*) Model schematic illustrating G-actin transport and polymerization in the "spillover" protrusion. (*B–D*) Spatial profiles of actin species (normalized by the total actin concentration at the leading edge) in the spillover protrusion at steady state for transport of G-actin to the leading edge by diffusion-only with constant diffusivity (*B*), diffusion (constant diffusivity) plus constant anterograde velocity (*C*), and diffusion-only with variable diffusivity that increases from the leading edge ($D_G(0) = 3$) rearward (*D*). (*E*) Kymographs of FRAP simulations where the entire span of the spillover is bleached for the constant diffusion-only (*top*) and diffusion aided by anterograde drift (*bottom*) cases. The G-actin concentration at the leading edge is ∼0 for the simulations shown. (*F*) Predictions of leading-edge FRAP of GFP-actin, normalized to the GFP-actin concentration at the leading edge at steady state, after a simulated full-bleach protocol. Graphs show simulations for normalized G-actin concentration at the leading edge equal to ∼0 (*solid curves*) and 0.1 (*dashed curves*). Units for D_G are $\mu m^2/s$. To see this figure in color, go online.

whether or not diffusion alone can explain the flux of G-actin. As an alternative, we considered the addition of anterograde, vectorial transport of G-actin to demonstrate how the recovery kinetics are affected (Fig. 4 *A*). We also considered model variations with certain assumptions relaxed.

To develop intuition about this modeling approach and its predictions, simple 1D model simulations were performed. As a baseline scenario, with which others will be compared, we considered the hypothetical assumptions that G-actin transport is by diffusion only and that the rate of F-actin polymerization is limited by the diffusion of G-actin

($g(0) = 0$). Hereafter, we refer to this pair of assumptions as diffusion-only, diffusion-limited (DODL). If we further assume for now that the G-actin diffusivity is constant, and taking typical, measurable values for our experimental system ($L = 10$ μm; $V_F = 0.2$ μm/s; $g(L) = 0.15$; $f(L) = 0.60$), the corresponding value of the G-actin diffusivity, $D_{G,DODL(c)}$, would need to be equal to 10.5 μm^2/s to match the flux of F-actin polymerization at the leading edge (Fig. 4 *B*). An alternative scenario is to assume diffusion only, with constant diffusivity $D_{G(c)}$, but allow nonzero polymerizable G-actin concentration at the leading edge ($g(0) > 0$). For example, this would be the case if capture of polymerizable G-actin were rate-limiting. Given the same measurable constraints, the estimated value of $D_{G(c)}$ for such a scenario is always greater than $D_{G,DODL(c)}$. For example, with an assumption that $g(0) = 0.1$, the value of the diffusivity $D_{G(c)}$ would need to be 29.7 μm^2/s to match the flux (Fig. 4 *B*).

Adding constant anterograde velocity (agnostic of mechanism) as another contribution to G-actin transport, under the same experimental constraints, allows the same flux to be achieved with a lower G-actin diffusivity (Fig. 4 *C*). For the same measurable inputs as above, transport-limited polymerization ($g(0) = 0$), and a diffusivity value of $D_{G(c)} = 3$ μm^2/s, a G-actin anterograde velocity of $V_{G(c)} = 0.89$ μm/s is required, and this estimate only increases by 0.2% when $g(0) = 0.1$ (Fig. 4 *C*). This is because advective flux does not depend on the concentration gradient, and, in these scenarios, advection contributes much more than diffusion throughout most of the domain (Péclet number $Pe \approx 3$). We also considered the possibility of DODL with position-dependent diffusivity, $D_{G,DODL}(x)$. With $D_{G,DODL}(0)$ set to 3 μm^2/s and the other parameters set to match experimental inputs, the G-actin profile is similar to the case of constant diffusivity plus advection (Fig. 4 *D*).

With the model parameterized, one can predict associated outcomes of FRAP experiments. With regard to modeling, the simplest protocol to interpret is the photobleaching of the entire nonadhesive zone. The corresponding 1D model was used to predict the recovery of unbleached actin for each of the five scenarios outlined above (Figs. 4 *E*, S1, and S2). The simulations predict distinct rates of recovery at the leading edge, assessed in terms of $t_{0.5}$, defined as the postbleach time at which leading-edge actin fluorescence had recovered to half of its prebleach value (Fig. 4 *F*). For our five example scenarios, the predicted $t_{0.5}$ values are: DODL (constant diffusivity): 1.7 s; diffusion-only, $g(0) = 0.1$: 1.2 s; $D_{G(c)} = 3$ μm^2/s, $g(0) = 0$: 5.6 s; $D_{G(c)} = 3$ μm^2/s, $g(0) = 0.1$: 6.6 s; and DODL (variable diffusivity) with $D_{G,DODL}(0) = 3$ μm^2/s: 1.5 s. For a given flux, reducing the diffusivity by allowing advection yields substantially slower recovery. In contrast, allowing variable diffusivity only slightly affects leading-edge recovery relative to the constant diffusivity case; this was true for other variable-diffusivity scenarios with either increasing or decreasing $D_{G,DODL}(x)$ (Fig. S3). Analysis of the DODL scenarios, based on the leading eigenvalue of the related Dirichlet problem (29), explains this finding; a recent mathematical analysis of the variable-diffusivity scenario (30) was key to helping us understand this result (see also Text S1, section 6).

As an addendum to this analysis, we also examined diffusion-only scenarios with two distinct G-actin states, relaxing the assumptions that G-actin states may be lumped with respect to transport properties and polymerizability (Text S1, sections 4 and 5). In one such scenario, we considered the possibility that a slowly diffusing pool of polymerizable actin is fed by rapid and spatially focused conversion from a fast-diffusing state, rather than by vectorial transport. Although such a scheme successfully flattens the steady-state G-actin gradient far from the leading edge, leading-edge FRAP is comparable with that of the simple DODL model (Fig. S4). In a second scenario, we considered that the two G-actin species have equal diffusivities, but conversion from a nonpolymerizing to a polymerizable state occurs at a modest frequency. Nevertheless, leading-edge FRAP is likewise comparable with that of the simple DODL model (Fig. S5).

Analysis of FRAP experiments consistently rules out G-actin transport by diffusion only

In the previous section, we showed how modeling can be used to test the common assumption that G-actin is transported by diffusion only. If the $t_{0.5}$ of leading-edge FRAP substantially exceeds that of the DODL prediction, constrained by flux-defining inputs from the particular experiment, it indicates that another transport mechanism is assisting diffusion. Here, we show the results of this test applied to the aforementioned cohort of seven cells (Fig. 5).

For each cell in the cohort, a rectangular zone containing a section of the leading-edge contour was selected and rapidly bleached. Experimental inputs were estimated to yield the prebleach, steady-state actin profile; this served as the initial condition for 2D simulations in which the position and dimensions of the bleach zone and the bleaching time were recreated as precisely as possible (Fig. 5 *A*). Scenarios corresponding to DODL (constant diffusivity) and various combinations of constant G-actin diffusivity and anterograde flow velocity were simulated, and the simulations were analyzed in the same fashion as for the corresponding experiment to construct leading-edge recovery profiles (Fig. 5 *B*). The representative cell showed recovery ($t_{0.5} = 3.8$ s) that was ~2.5-fold slower than the DODL (constant diffusivity) scenario; the recovery was reasonably consistent with a lower constant diffusivity and advection added ($D_{G(c)} = 2$ μm^2/s and $V_{G(c)} = 0.55$ μm/s). For this cell, comparison of the total actin intensity profiles, quantified at a postbleach time approximately equal to $2^*t_{0.5}$, likewise shows the best agreement with the $D_{G(c)} = 2$ μm^2/s

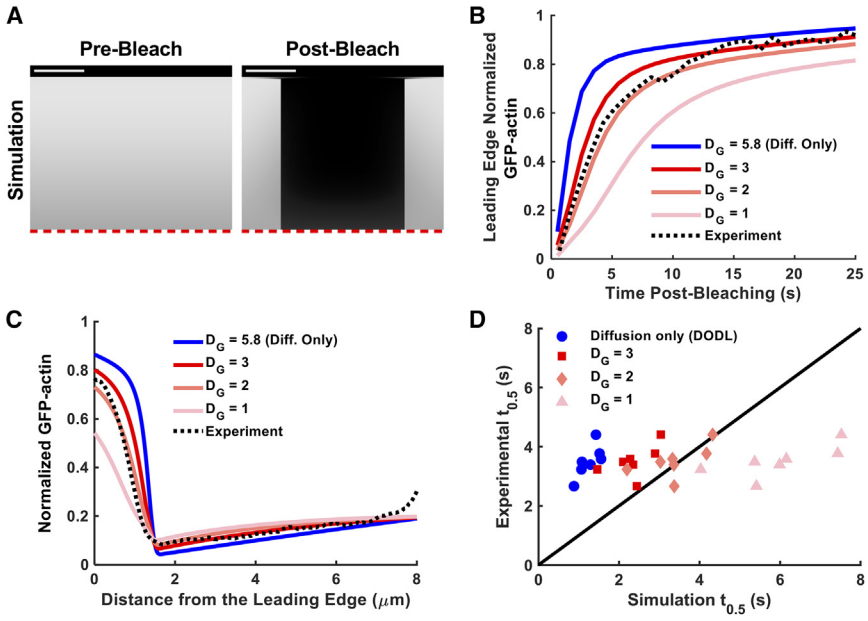

FIGURE 5 Model-guided analysis of FRAP experiments consistently rules out anterograde transport of G-actin by diffusion only. (*A*) Two-dimensional model simulations were parameterized to yield a prebleach steady-state actin profile comparable with the corresponding movie. The spatiotemporal bleaching protocol was replicated as closely as possible accounting for bleach area, bleach duration, and associated equipment processing time. Scale bar, 3 μm. (*B*) Graph of the fluorescence recovery of GFP-actin at the leading edge for the representative movie shown in (*A*) along with the corresponding model predictions for different parameterizations of G-actin diffusion and anterograde velocity. (*C*) Graph of the spatial profile of GFP-actin spanning the spillover protrusion at time = $2*t_{0.5}$ postphotobleaching for the representative movie shown in (*A*) and the corresponding model simulations. (*D*) Graph of the experimental $t_{0.5}$ values, for each of the movies in the cohort ($n = 7$), plotted against the corresponding predictions of $t_{0.5}$ values from simulations with different parameterizations of G-actin diffusion and anterograde velocity. To see this figure in color, go online.

scenario (Fig. 5 *C*). This finding was consistent for all of the cells in the cohort (Fig. 5 *D*). The ratios of $t_{0.5}$ (experimental) to $t_{0.5}$ (DODL simulation) ranged from 2.3 to 3.2, and spatial profiles were also compared (Fig. S6). We conclude that the assumption that G-actin transport is by diffusion alone grossly and consistently fails to predict the arrival of unbleached G-actin in our system.

Whether after photobleaching the full or partial span of the nonadhesive region, we saw rapid incorporation of bleached actin into F-actin, manifest as a thin, dark band extending out beyond the lateral boundaries of the bleached area (Fig. 2 *A*). Simulated FRAP predictions are qualitatively consistent with those observations, and they indicate certain quantitative differences between DODL versus diffusion plus advection scenarios (Fig. S7); however, various methods devised to quantify those features from experimental time series proved to be insufficiently robust.

Inhibition of actin polymerization elicits accumulation of G-actin at the leading edge

Our modeling efforts suggest a possible vectorial transport mechanism contributing to the supply of actin monomers for actin polymerization at the leading edge. Thus, one might predict an accumulation or enrichment of G-actin at the leading edge upon the stalling of F-actin polymerization in our experimental model. To test this prediction, we treated cells plated on the Fn micropatterns with CytoD (1 μM) to abruptly halt F-actin polymerization by blocking barbed end elongation, and we monitored the changes in the GFP-actin intensity in the spillover region. CytoD treatment stalled F-actin polymerization, resulting in withdrawal and condensation of the F-actin network, leading to a large drop in GFP-actin intensity at the leading edge; shortly thereafter, a thin ($\sim$1 μm) band of GFP-actin signal appeared there (Fig. 6 *A*; Video S5). Kymographs show that this signal was stationary with respect to the leading edge and increased in intensity with time over the course of $\sim$1 min (Fig. 6, *B* and *C*). Every treated cell showed such recovery of the leading-edge intensity (Fig. 6 *D*). When leading-edge regions of CytoD-treated cells were photobleached, FRAP was near-complete ($\sim$85% mean mobile fraction), with kinetics that were consistent with the prior appearance of the GFP-actin band ($\sim$50 s mean half-time) (Fig. S8). The CytoD-induced effects were simulated, under DODL and diffusion plus vectorial transport scenarios, by assuming that the fluxes at the leading edge suddenly vanish. Consistent with the experimental observations, G-actin is predicted to accumulate at the boundary, with a timescale of $\sim$1 min, when advection is included; in contrast, such a gradient of G-actin cannot be established if its transport is by diffusion only (Fig. 6, *E* and *F*).

DISCUSSION

Cell migration is a dynamic process involving both biochemical (signal transduction and actin dynamics) and mechanical (cell adhesion/traction, membrane protrusion, and contractility) subprocesses. Leading-edge motility and cell shape changes are stochastic and unpredictable, reflecting nonlinearities that have been attributed to positive and negative feedback loops and excitability (26,31–34). This makes cell migration a rich yet challenging phenomenon to study. To reduce complexity, an informative approach to study actin dynamics in particular has been to isolate the effects of certain interactions among purified proteins.

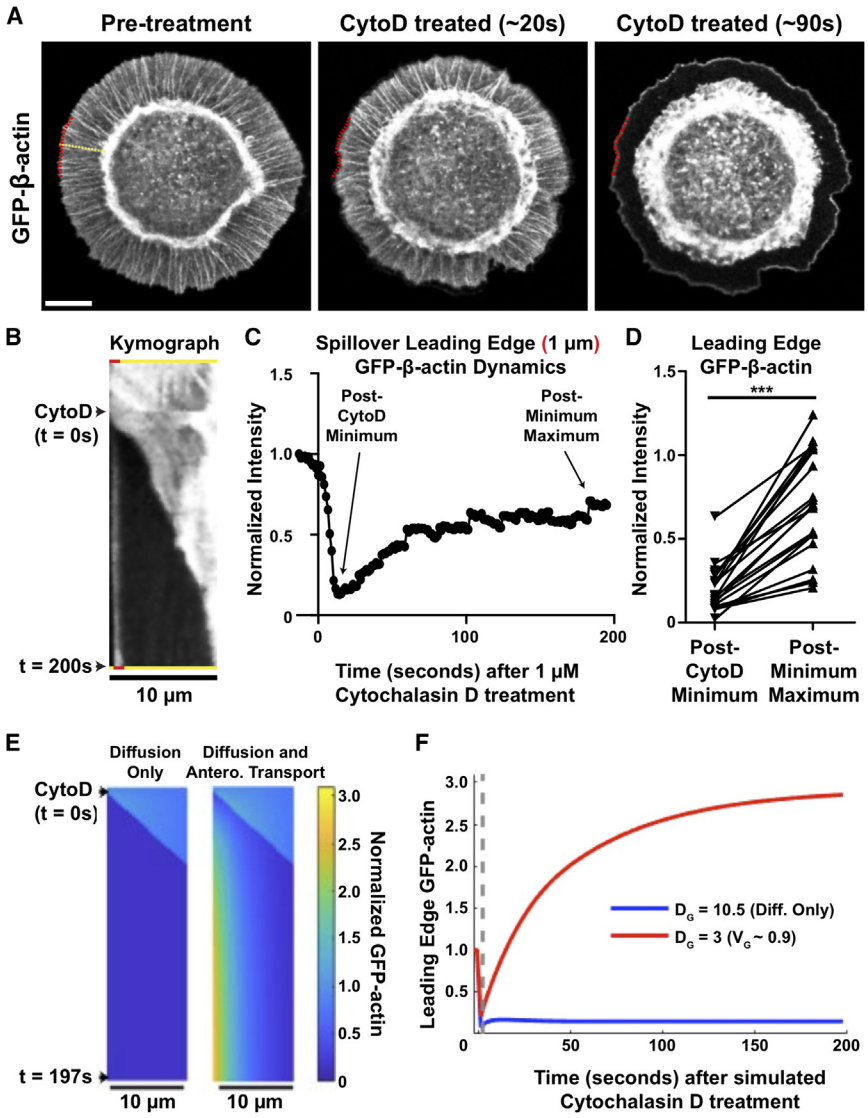

FIGURE 6 GFP-actin accumulates at the very leading edge of spillover protrusions upon inhibition of F-actin polymerization. (*A*) Still images of a JR20 Fibroblast expressing GFP-actin and plated on micropatterned Fn island as detailed in Fig. 1*A* before and after treatment with 1 μM cytochalasin D (CytoD). The dashed yellow line is representative of a region kymographs were generated from, and the dashed red line marks the ~1 μm distal-most region of spillover protrusion that intensity measurements were taken from. Scale bar, 10 μm. (*B*) Kymograph of a spillover protrusion labeled with GFP-actin in the cell shown in (*A*), with the distal-most region marked by the red rectangles at the top and bottom of the kymograph. (*C*) Quantification of spillover leading edge GFP-actin intensity before and after 1 μM CytoD treatment of the cell shown in (*A*) normalized to the intensity ~13 s pretreatment (10 frames). (*D*) Minimum GFP-actin intensity at the edge of spillover protrusions after 1 μM CytoD treatment with a connecting line to the maximum GFP-actin intensity that accumulates in the same roughly 10 × 1 μm region a short time afterward. Each pair of measurements comes from a single cell plated on a unique micropatterned coverslip ($n = 20$ cells across 5 independent experiments). $p < 0.0001$ (paired *t*-test). (*E* and *F*) In 1D simulations parameterized as in Fig. 4, *B* and *C*, with $g(0) \approx 0$, CytoD treatment was mimicked by switching the leading-edge boundary conditions to zero flux. Simulated kymographs (*E*) and leading-edge kinetics (*F*) of GFP-actin intensity are shown. To see this figure in color, go online.

The hope is that the knowledge gained from such careful measurements may be stitched together in a conceptual and mathematical modeling framework (32–34).

Here, we describe an experimental system that presents a compromise between observing dynamics as they occur in cells and measuring kinetics in a simplified system. By limiting the area of adhesive contact between a cell and the substratum, the cell's lamellipodium is forced to spill over into the nonadhesive area, with a morphology that is remarkably steady and consistent in dimensions. In this region, actin polymerization is ~3 times faster than measured in the same cell line when randomly migrating, which might be attributed to the lack of adhesion complexes that would otherwise clutch the network and resist/dissipate retrograde flow (35), and to reduced mechanical load on elongating barbed ends at the approximately stationary boundary. Accordingly, the retrograde flow velocity is approximately constant as F-actin travels from the leading edge to the nonadhesive/adhesive interface; along the way, actin depolymerization is modest, and so the bulk of the F-actin is disassembled at the interface, where it is seized by myosin II. Therefore, most actin monomers must traverse the full span of the nonadhesive region before reincorporation into F-actin.

The combination of fast actin polymerization and low G-/F-actin ratio per volume within the nonadhesive region led us to question whether or not the required G-actin flux is achieved by diffusion alone in our system. Within the thin lamellipodial protrusion, the F-actin mesh impedes macromolecular transport, with excluded volume and nonspecific interaction effects contributing (36–38). Indeed, our robust estimates of the minimum G-actin diffusivity required are at the high end of the range of published estimates (~1–10 $\mu m^2/s$) (11–13,39–43). Through design, analysis, and

simulation of FRAP experiments, we found that the assumption that G-actin is transported by diffusion only grossly and consistently fails to predict recovery. This was the case even when G-actin diffusivity was allowed to vary with position, potentially due to gradients of F-actin mesh porosity and/or of G-actin interactions (both specific and nonspecific), or when two states of G-actin with different diffusivities or propensities to polymerize were simulated. By comparison, a G-actin transport model with diffusivity $\approx 2\ \mu m^2/s$ and constant anterograde velocity less than 1 μm/s yielded good agreement. To explain this, we consider that, at early times postbleach, there is a steep, positive gradient of unbleached G-actin and an almost-as-steep, negative gradient of bleached G-actin in the x-direction. These sum to maintain the relatively modest, positive gradient of G-actin overall. Therefore, at early times postbleach, the flux of unbleached G-actin is much greater than at steady state and dominated by diffusion. Slowing down the diffusion is the key to slowing down FRAP, while adding anterograde, vectorial transport allows the steady-state flux to be achieved.

While we are currently not in a position to speculate on the precise nature of vectorial G-actin transport, related discussions in the literature have centered on motor-driven transport and bulk fluid flow as ways to enhance G-actin transport in lamellipodia. With regard to the action of motors, anterograde transport of G-actin has been attributed to direct interaction with Myo1c (14), but it is presently unclear whether this interaction can account for the inferred magnitude of the velocity. On the other hand, the bulk fluid flow concept is related to the hypothesis that actin disassembly by myosin II can generate a significant gradient in osmotic pressure (13,44–46), with water leaking out of the cell courtesy of aquaporin channels (46–48). The anterograde velocity cited above corresponds to an estimated, overall volumetric flow rate of $\sim$10 fL/s. With an estimated rate of $\sim 10^9$ water molecules per channel per second, such a flow rate might be achieved by only a few hundred aquaporin molecules.

Acute disruption of F-actin barbed end elongation by CytoD led to the expected retrograde withdrawal of the F-actin network from the spillover protrusion, but also later led to the appearance of a stationary band of GFP-actin intensity at the extreme leading edge of the protrusion. We postulate that this GFP-actin fluorescence represents G-actin that has accumulated at the leading edge in a futile manner, without barbed ends on which to polymerize. While this result is consistent with vectorial transport contributing to G-actin recycling, it is important to interpret this result carefully. For example, treatment with CytoD causes substantial rearrangements of all F-actin networks in the cell, and this could disrupt or alter some of the aforementioned mechanisms of bulk transport, such as myosin-based contractility. Another possibility worth considering is that stalled actin polymerases such as formins or Ena/VASP proteins may concentrate monomeric GFP-actin at the leading edge upon CytoD treatment. Future experiments and modeling will tackle these and other possibilities.

To the extent that bulk fluid flow contributes significantly to G-actin transport, two conjectures arise. The first is that asymmetries of the cell geometry and of the osmotic pressure would render the assumption of a constant, unidirectional flow implausible. Complex, multidirectional flow should be expected. The second is that the constrained adhesion drives the enrichment of actomyosin at the nonadhesive/adhesive interface that, in turn, drives bulk flow. If so, it would be fair to ask how such an osmotic pressure gradient might differ across experimental contexts, depending on the spatial organization of myosin II activity. More generally, the broad variety of cell migration/actin-based motility phenotypes displayed by different cell types presents an inherent limitation of any experimental system in this field.

Related to the above, we also acknowledge certain limitations of the mathematical modeling and model-based analysis presented here. The model used to directly compare with experimental data invokes certain simplifying assumptions, which were explored through ancillary simulations and specific variations of the model. We critically evaluated assumptions concerning the boundary conditions used for FRAP predictions and considered two distinct pools of G-actin (12). Although none of these variations substantially alter the prediction of leading-edge FRAP when G-actin transport is by diffusion only, refinements of the model should be considered when additional evidence or the experimental context warrants. Another model assumption, based on experimental observations in fibroblasts, was to neglect local reincorporation of actin into filaments at sites other than the leading edge; this is noteworthy because it stands in direct contrast with indications from other studies (27,28,43). Although local polymerization no doubt occurs at some rate in our system, the observed patterns of FRAP in the bleached region support our assumption. If actin were somehow reincorporated at a substantial rate but without perceptible image texture, the consequence would be an overestimation of the relative G-actin concentration distal from the leading edge; some of the measured intensity attributed to G-actin would be in the form of F-actin. In that case, the value of the diffusivity that matches the required steady-state flux for a diffusion-only scenario would need to be higher, contributing to a faster leading-edge FRAP.

The experimental and modeling framework established here can be used to evaluate and make quantitative predictions for future experimental approaches, as well as to explore other biological questions concerning actin network dynamics. Previous studies have used photoconvertible actin probes (12) or tagged, but nonpolymerizable actin mutant proteins (14) to test the mechanisms of G-actin transport, and it will be useful in future work to compare those approaches with the FRAP approach in our system. The spillover protrusion system is ripe to explore other

aspects of actin filament network dynamics such as the relative contributions of branched versus unbranched actin polymerization, the role of NMII in network turnover, and the roles of profilin and other actin monomer binding proteins in transport and polymerization/depolymerization.

SUPPORTING MATERIAL

Supporting material can be found online at https://doi.org/10.1016/j.bpj.2023.08.022.

AUTHOR CONTRIBUTIONS

R.A. designed research, performed research, analyzed data, and wrote and edited the paper. M.T.B. designed research, performed research, analyzed data, and wrote and edited the paper. J.E.B. was responsible for conceptualization, research design, supervision, funding acquisition, and wrote and edited the paper. J.M.H. was responsible for conceptualization, research design, data analysis, supervision, funding acquisition, and wrote and edited the paper.

ACKNOWLEDGMENTS

We acknowledge Dr. David M. Graham for methodological developments and initial observations that led to this work, Matthew Farkas (University of Washington) for helpful discussions about his work on heat transfer with variable conductivity, and Drs. Les Loew and Boris Slepchenko for helpful discussions about numerical model implementation. We also wish to express our gratitude to the late Prof. Ken Jacobson, whose mentoring and pioneering applications of FRAP and mathematical modeling to cell biology truly inspired this work. Research reported in this publication was supported by the National Institute of General Medical Sciences under award nos. R01 GM141691 (to J.M.H.) and R35 GM130312 (to J.E.B.), and by the National Institute of Biomedical Imaging and Bioengineering of the National Institutes of Health under award no. U01 EB018816 (to J.M.H.). The use of VCell software is supported by the National Institute of General Medical Sciences under award no. R24 GM137787. The content is solely the responsibility of the authors and does not necessarily represent the official views of the National Institutes of Health.

DECLARATION OF INTERESTS

The authors declare no competing interests.

REFERENCES

1. Pollard, T. D., and J. A. Cooper. 2009. Actin, a central player in cell shape and movement. *Science.* 326:1208–1212.
2. Svitkina, T. M., and G. G. Borisy. 1999. Arp2/3 complex and actin depolymerizing factor/cofilin in dendritic organization and treadmilling of actin filament array in lamellipodia. *J. Cell Biol.* 145:1009–1026.
3. Mogilner, A., and G. Oster. 1996. Cell motility driven by actin polymerization. *Biophys. J.* 71:3030–3045.
4. Lai, F. P. L., M. Szczodrak, …, K. Rottner. 2008. Arp2/3 complex interactions and actin network turnover in lamellipodia. *EMBO J.* 27:982–992.
5. Lappalainen, P., T. Kotila, …, G. Romet-Lemonne. 2022. Biochemical and mechanical regulation of actin dynamics. *Nat. Rev. Mol. Cell Biol.* 23:836–852.
6. Wioland, H., B. Guichard, …, G. Romet-Lemonne. 2017. ADF/Cofilin Accelerates Actin Dynamics by Severing Filaments and Promoting Their Depolymerization at Both Ends. *Curr. Biol.* 27:1956–1967.e7.
7. Wilson, C. A., M. A. Tsuchida, …, J. A. Theriot. 2010. Myosin II contributes to cell-scale actin network treadmilling through network disassembly. *Nature.* 465:373–377.
8. Funk, J., F. Merino, …, P. Bieling. 2019. Profilin and formin constitute a pacemaker system for robust actin filament growth. *Elife.* 8, e50963.
9. Li, T.-D., P. Bieling, …, D. A. Fletcher. 2022. The molecular mechanism of load adaptation by branched actin networks. *Elife.* 11, e73145.
10. Prass, M., K. Jacobson, …, M. Radmacher. 2006. Direct measurement of the lamellipodial protrusive force in a migrating cell. *J. Cell Biol.* 174:767–772.
11. Novak, I. L., B. M. Slepchenko, and A. Mogilner. 2008. Quantitative analysis of G-actin transport in motile cells. *Biophys. J.* 95:1627–1638.
12. Vitriol, E. A., L. M. McMillen, …, J. Q. Zheng. 2015. Two functionally distinct sources of actin monomers supply the leading edge of lamellipodia. *Cell Rep.* 11:433–445.
13. Zicha, D., I. M. Dobbie, …, G. A. Dunn. 2003. Rapid actin transport during cell protrusion. *Science.* 300:142–145.
14. Fan, Y., S. M. Eswarappa, …, P. L. Fox. 2012. Myo1c facilitates G-actin transport to the leading edge of migrating endothelial cells. *J. Cell Biol.* 198:47–55.
15. Bear, J. E., and J. M. Haugh. 2014. Directed migration of mesenchymal cells: where signaling and the cytoskeleton meet. *Curr. Opin. Cell Biol.* 30:74–82.
16. Azioune, A., M. Storch, …, M. Piel. 2009. Simple and rapid process for single cell micro-patterning. *Lab Chip.* 9:1640–1642.
17. Michalski, P. J., and A. E. Carlsson. 2010. The effects of filament aging and annealing on a model lamellipodium undergoing disassembly by severing. *Phys. Biol.* 7, 026004.
18. Mogilner, A., and B. Rubinstein. 2010. Actin disassembly "clock" and membrane tension determine cell shape and turning: a mathematical model. *J. Phys. Condens. Matter.* 22, 194118.
19. Barnhart, E. L., K.-C. Lee, …, J. A. Theriot. 2011. An adhesion-dependent switch between mechanisms that determine motile cell shape. *PLoS Biol.* 9, e1001059.
20. Ni, Q., and G. A. Papoian. 2019. Turnover versus treadmilling in actin network assembly and remodeling. *Cytoskeleton (Hoboken).* 76:562–570.
21. Perelroizen, I., J. B. Marchand, …, M. F. Carlier. 1994. Interaction of profilin with G-actin and poly(L-proline). *Biochemistry.* 33:8472–8478.
22. Perelroizen, I., M. F. Carlier, and D. Pantaloni. 1995. Binding of divalent cation and nucleotide to G-actin in the presence of profilin. *J. Biol. Chem.* 270:1501–1508.
23. Breitsprecher, D., A. K. Kiesewetter, …, J. Faix. 2011. Molecular mechanism of Ena/VASP-mediated actin-filament elongation. *EMBO J.* 30:456–467.
24. Cowan, A. E., I. I. Moraru, …, L. M. Loew. 2012. Spatial modeling of cell signaling networks. *Methods Cell Biol.* 110:195–221.
25. Ferziger, J. H., and M. Perić. 2002. Computational Methods for Fluid Dynamics. Springer Berlin Heidelberg.
26. Chandra, A., M. T. Butler, …, J. M. Haugh. 2022. Modeling cell protrusion predicts how myosin II and actin turnover affect adhesion-based signaling. *Biophys. J.* 121:102–118.
27. Watanabe, N., and T. J. Mitchison. 2002. Single-molecule speckle analysis of actin filament turnover in lamellipodia. *Science.* 295:1083–1086.
28. Raz-Ben Aroush, D., N. Ofer, …, K. Keren. 2017. Actin Turnover in Lamellipodial Fragments. *Curr. Biol.* 27:2963–2973.e14.
29. Deen, W. M. 2012. Analysis of Transport Phenomena, 2nd ed. Oxford University Press.
30. Farkas, M., and B. Deconinck. 2023. Solving the heat equation with variable thermal conductivity. *Appl. Math. Lett.* 135, 108395.

31. Kunida, K., M. Matsuda, and K. Aoki. 2012. FRET imaging and statistical signal processing reveal positive and negative feedback loops regulating the morphology of randomly migrating HT-1080 cells. *J. Cell Sci.* 125:2381–2392.
32. Krause, M., and A. Gautreau. 2014. Steering cell migration: lamellipodium dynamics and the regulation of directional persistence. *Nat. Rev. Mol. Cell Biol.* 15:577–590.
33. Devreotes, P. N., S. Bhattacharya, …, Y. Miao. 2017. Excitable Signal Transduction Networks in Directed Cell Migration. *Annu. Rev. Cell Dev. Biol.* 33:103–125.
34. Michaud, A., Z. T. Swider, …, W. M. Bement. 2021. Cortical excitability and cell division. *Curr. Biol.* 31:R553–R559.
35. Craig, E. M., J. Stricker, …, A. Mogilner. 2015. Model for adhesion clutch explains biphasic relationship between actin flow and traction at the cell leading edge. *Phys. Biol.* 12, 035002.
36. Luby-Phelps, K. 2000. Cytoarchitecture and physical properties of cytoplasm: volume, viscosity, diffusion, intracellular surface area. *Int. Rev. Cytol.* 192:189–221.
37. Baboolal, T. G., G. I. Mashanov, …, J. E. Molloy. 2016. A Combination of Diffusion and Active Translocation Localizes Myosin 10 to the Filopodial Tip. *J. Biol. Chem.* 291:22373–22385.
38. Novak, I. L., P. Kraikivski, and B. M. Slepchenko. 2009. Diffusion in cytoplasm: effects of excluded volume due to internal membranes and cytoskeletal structures. *Biophys. J.* 97:758–767.
39. Kiuchi, T., T. Nagai, …, K. Mizuno. 2011. Measurements of spatiotemporal changes in G-actin concentration reveal its effect on stimulus-induced actin assembly and lamellipodium extension. *J. Cell Biol.* 193:365–380.
40. Sehayek, S., X. Yi, …, P. W. Wiseman. 2021. Rapid ensemble measurement of protein diffusion and probe blinking dynamics in cells. *Biophys. Rep.* 1, 100015.
41. McGrath, J. L., Y. Tardy, …, J. H. Hartwig. 1998. Simultaneous measurements of actin filament turnover, filament fraction, and monomer diffusion in endothelial cells. *Biophys. J.* 75:2070–2078.
42. Roy, P., Z. Rajfur, …, K. Jacobson. 2001. Local photorelease of caged thymosin beta4 in locomoting keratocytes causes cell turning. *J. Cell Biol.* 153:1035–1048.
43. Smith, M. B., T. Kiuchi, …, D. Vavylonis. 2013. Distributed actin turnover in the lamellipodium and FRAP kinetics. *Biophys. J.* 104:247–257.
44. Zhu, C., and R. Skalak. 1988. A continuum model of protrusion of pseudopod in leukocytes. *Biophys. J.* 54:1115–1137.
45. Iwasaki, T., and Y.-L. Wang. 2008. Cytoplasmic force gradient in migrating adhesive cells. *Biophys. J.* 94:L35–L37.
46. Keren, K., P. T. Yam, …, J. A. Theriot. 2009. Intracellular fluid flow in rapidly moving cells. *Nat. Cell Biol.* 11:1219–1224.
47. Verkman, A. S. 2011. Aquaporins at a glance. *J. Cell Sci.* 124:2107–2112.
48. Loitto, V. M., C. Huang, …, K. Jacobson. 2007. Filopodia are induced by aquaporin-9 expression. *Exp. Cell Res.* 313:1295–1306.

Biophysical Journal, Volume *122*

Supplemental information

G-actin diffusion is insufficient to achieve F-actin assembly in fast-treadmilling protrusions

Ravikanth Appalabhotla, Mitchell T. Butler, James E. Bear, and Jason M. Haugh

Supporting Information

'G-actin diffusion is insufficient to achieve F-actin assembly in fast-treadmilling protrusions,' by Appalabhotla et al.

Text S1: Modeling Supplement

Supplemental Figures

Captions for Supplemental Movies S1-S5

Text S1: Modeling Supplement

1. General results for derivation of the general steady-state (pre-bleach) model

Our model is cast in terms of total G- and F-actin, which can exist in a variety of nucleotide- and regulatory protein-bound states. Here, we formulate the model with an accounting of all cytosolic states of G-actin, all states of F-actin, and all leading-edge membrane-bound states of G-actin. Modeling assumptions will be stated as they are invoked, so that the reader will know the generality of each set of equations.

Assumption 1.1: The cytoplasm of the non-adhesive region is homogenized into a single, continuous phase.

With this established, we define the cytosolic concentrations of G- and F-actin in various states i and j, respectively; their fluxes; the densities of leading-edge membrane-bound G-actin in various states n; and all of the sums thereof:

$$G = \sum_i G_i\,; \quad F = \sum_j F_j\,;$$

$$\mathbf{N}_G = \sum_i \mathbf{N}_{G,i}\,; \quad \mathbf{N}_F = \sum_j \mathbf{N}_{F,j}\,;$$

$$G_m = \sum_n G_{m,n}.$$

Because all F-actin moves together via retrograde flow, we can define the fluxes for each F-actin species and for total F-actin:

$$\mathbf{N}_{F,j} = \mathbf{V}_F F_j; \quad \mathbf{N}_F = \mathbf{V}_F F,$$

where $\mathbf{V}_F$ is the F-actin retrograde flow velocity vector (experienced by all F-actin species j). Next, rate terms are defined in order to construct the general conservation equations, with:

Assumption 1.2: Within the non-adhesive domain, rates of GFP-β-actin synthesis and degradation are negligible relative to those affecting actin dynamics.

Neglecting such terms, the bookkeeping equations are

$$\frac{\partial G_i}{\partial t} = -\nabla \cdot \mathbf{N}_{G,i} - \sum_j \left(r_{pol,ij} - r_{depol,ij}\right) + \sum_{k \neq i} \left(r_{interG,ki} - r_{interG,ik}\right);$$

$$\frac{\partial F_j}{\partial t} = -\nabla \cdot \mathbf{N}_{F,i} + \sum_i \left(r_{pol,ij} - r_{depol,ij}\right) + \sum_{k \neq j} \left(r_{interF,kj} - r_{interF,jk}\right);$$

$$\frac{dG_{m,n}}{dt} = \sum_i \left(r_{on,in} - r_{off,in}\right) - \sum_j r_{pol,m,nj} + \sum_{k\neq n} \left(r_{interM,kn} - r_{interM,nk}\right).$$

The rates are defined as:
$r_{pol,ij}$ is the rate of polymerization of G-actin species i to form F-actin species j;
$r_{depol,ij}$ is the rate of depolymerization of F-actin species j to form G-actin species i;
$r_{interG,ki}$ is the rate of interconversion from G-actin species $k \neq i$ to generate G-actin species i;
$r_{interF,kj}$ is the rate of interconversion from F-actin species $k \neq j$ to generate F-actin species j;
$r_{on,in}$ is the rate of G-actin species i association to form membrane-bound species n;
$r_{off,in}$ is the rate of G-actin species i dissociation from membrane-bound species n;
$r_{pol,m,nj}$ is the rate of G-actin transfer from membrane-bound species n to form F-actin species j; and
$r_{interM,kn}$ is the rate of interconversion from membrane-bound species $k \neq n$ to generate membrane-bound species n.
Flux balances at $x = 0$ are

$$N_{x,G,i}\big|_{x=0} = -\sum_n \left(r_{on,in} - r_{off,in}\right) - \sum_j N_{pol,c,ij};$$
$$N_{x,F,j}\big|_{x=0} = \sum_i N_{pol,c,ij} + \sum_n r_{pol,m,nj}.$$

Here, $N_{x,G,i}$ is the x-component of the flux for G-actin species i, $N_{x,F,j}$ is the x-component of the flux for F-actin species j, and $N_{pol,c,ij}$ is the flux of G-actin species i incorporation to form F-actin species j, directly from the cytosol. By summing these, we obtain

$$\frac{\partial G}{\partial t} = -\nabla \cdot \mathbf{N}_G - r_{pol} + r_{depol};$$
$$\frac{\partial F}{\partial t} = -\nabla \cdot \mathbf{N}_F + r_{pol} - r_{depol};$$
$$\frac{dG_m}{dt} = r_{on} - r_{off} - r_{pol,m};$$
$$N_{x,G}\big|_{x=0} = -r_{on} + r_{off} - N_{pol,c}; \quad N_{x,F}\big|_{x=0} = N_{pol,c} + r_{pol,m},$$

where

$$r_{pol} = \sum_i \sum_j r_{pol,ij}; \quad r_{depol} = \sum_i \sum_j r_{depol,ij};$$

$$r_{on} = \sum_n \sum_i r_{on,in}\,; \quad r_{off} = \sum_n \sum_i r_{off,in}\,; \quad r_{pol,m} = \sum_n \sum_j r_{pol,m,nj}\,;$$
$$N_{pol,c} = \sum_i \sum_j N_{pol,c,ij}.$$

Assumption 1.3: The system is at steady state:

$$\frac{\partial G_i}{\partial t} = \frac{\partial F_j}{\partial t} = \frac{dG_{m,n}}{dt} = 0.$$

With the densities of the membrane-bound states at steady state, we obtain

$$N_{x,F}\big|_{x=0} = -N_{x,G}\big|_{x=0} = N_{pol} = N_{pol,c} + r_{pol,m};$$

and, because the total actin in the cytosol (G- plus F-) is conserved,

$$\nabla \cdot (\mathbf{N}_G + \mathbf{N}_F) = 0.$$

Assumption 1.4: Gradients of total G- and F-actin are negligible in the y- and z-directions.

Hence, we can write

$$N_{x,G}(x) + N_{x,F}(x) = 0.$$

In the main text, we simplify the notation, with $N_{x,G} \to N_G$ and $N_{x,F} \to N_F$.

2. Additional analysis of FRAP model boundary conditions: $x = 0$

In the previous section we showed that, at steady state, the kinetics and spatial variations of G-actin nucleotide exchange, complex formation at the leading edge, and incorporation into F-actin need not be considered. In contrast, to predict FRAP kinetics, these aspects do need to be considered, especially as they relate to the boundary conditions for F- and G-actin at the leading edge ($x = 0$). Continuing from the preceding Section 1, additional assumptions used to formulate those boundary conditions will be stated as they are used.

The generalized fluxes of unbleached G- and F-actin at $x = 0$ are as follows; see the previous section for definitions.

$$N_{Gun}|_{x=0} = -\sum_i \left[\sum_n \left(r_{on,in} \frac{G_{un,i}}{G_i}\bigg|_{x=0} - r_{off,in} \frac{G_{mun,n}}{G_{m,n}} \right) - \sum_j N_{pol,c,ij} \frac{G_{un,i}}{G_i}\bigg|_{x=0} \right];$$
$$N_{Fun}|_{x=0} = \sum_j \left(\sum_i N_{pol,c,ij} \frac{G_{un,i}}{G_i}\bigg|_{x=0} + \sum_n r_{pol,m,nj} \frac{G_{mun,n}}{G_{m,n}} \right).$$

We proceed to write generalized unsteady balances for the unbleached forms of the membrane-bound species, valid after bleaching, after stating:

Assumption 2.1: Interconversion between membrane-bound states (e.g., nucleotide exchange) occurs at rates that are negligible compared to the rates of dissociation and elongation.

$$\frac{dG_{mun,n}}{dt} = \sum_i \left(r_{on,in} \frac{G_{un,i}}{G_i}\bigg|_{x=0} \right) - \left(\sum_i r_{off,in} + \sum_j r_{pol,m,nj} \right) \frac{G_{mun,n}}{G_{m,n}}.$$

With this formulation, we see that the mean lifetime of an unbleached G-actin molecule in membrane-bound state n is

$$\tau_n = \frac{G_{m,n}}{\sum_i r_{off,in} + \sum_j r_{pol,m,nj}}.$$

Assumption 2.2: $G_{mun,n}$ are quasi-steady, an approximation we consider valid for $t \gg \tau_n$.

Hence, we obtain

$$\frac{G_{mun,n}}{G_{m,n}} \approx \frac{\sum_i \left(r_{on,in} \frac{G_{un,i}}{G_i}\Big|_{x=0} \right)}{\sum_i r_{off,in} + \sum_j r_{pol,m,nj}} = \frac{\sum_i \left(r_{on,in} \frac{G_{un,i}}{G_i}\Big|_{x=0} \right)}{\sum_i r_{on,in}}.$$

Incorporating this result into the flux expressions, we obtain

$$-N_{Gun}|_{x=0} = N_{Fun}|_{x=0} = \sum_j \sum_i \left[\left(N_{pol,c,ij} + \sum_n r_{pol,m,nj} \frac{r_{on,in}}{\sum_i r_{on,in}} \right) \frac{G_{un,i}}{G_i}\bigg|_{x=0} \right].$$

Assumption 2.3: The soluble G-actin species at the leading edge are equally polymerizable.

Hence, we obtain the result used to formulate the boundary conditions in the text:

$$-N_{Gun}(0,t) = N_{Fun}(0,t) = \sum_j \left(N_{pol,c,ij} + \sum_n r_{pol,m,nj} \right) \frac{G_{un}}{G}\bigg|_{x=0} = N_{pol} \frac{G_{un}}{G}\bigg|_{x=0}.$$

With that done, we address now the validity of the three assumptions introduced in this section. The first two are readily addressed, considering published frequencies of profilin-G-actin dissociation and profilin-mediated transfer from polymerases (> 10 s^{-1}; references cited in the main text). By comparison, we acknowledge that the latter assumption is least general. It is accurate for scenarios with diffusion-limited polymerization ($g_{un}(0) \approx 0$); in that case, the boundary condition is equivalent to a Dirichlet boundary condition for g_{un} and flux-matching for f_{un}:

$$f_{un}(0,t) = \frac{D_G}{V_F}\frac{\partial g_{un}}{\partial x}\bigg|_{x=0} \quad \text{(diffusion-limited)}.$$

On the other hand, the assumption is not expected to be accurate for scenarios in which conversion to a polymerizable state of G-actin might be sluggish. We explore such a scenario in Section 5 of this supplement.

3. Additional analysis of FRAP model boundary conditions: $x = L$

In the main figures of the paper, FRAP predictions applied a Dirichlet (constant-value) boundary condition at $x = L$, assuming that the unbleached G-actin concentration there is maintained at the pre-bleach value:

$$g_{un}(L, y, t) = g(L).$$

The justification stated in the text is that the rear of the bleach zone backs up to the bulk of the cell volume and to a concentrated depot of disassembling F-actin. While we consider this assumption reasonable, we recognize that it represents an asymptotic limit of the true dynamics at that location, which is subject to diffusion of bleached G-actin into the cell body. In this section, we show that relaxing the constant-value assumption only modestly affects the prediction.

To address this, we constructed a 3D model in VCell that approximates the geometry of a cell adhered to a circular region of 30-μm diameter: a hemispherical (radius = 15 μm) cell body connected to a non-adhesive ring (outer radius = 25 μm, corresponding to L = 10 μm) (**Fig. S1A**). The lone species in this model is G-actin; to achieve a steady-state G-actin concentration field, G-actin is consumed by a 'sink' species confined to the membrane within the outermost 0.1 μm of the domain, and it is generated from a 'source' species confined to a ring on the bottom membrane with inner and outer radii of 14 and 15 μm at the interface between the cell body and non-adhesive region (**Fig. S1A**). The sink reaction is first-order with respect to G-actin concentration and sufficiently fast to drive the G-actin concentration to a very low value at the leading edge. The source reaction provides a constant flux, which determines the (arbitrary) scale of the concentration. VCell simulations were performed using the Fully-Implicit Finite Volume (variable time step) solver and a spatial discretization of 0.1 x 0.1 x 0.1 μm.

To closely match the two foundational scenarios presented in main **Fig. 4**, simulations were performed with 1) G-actin diffusivity $D_{G(c)}$ = 10.5 μm^2/s throughout the volume; and 2) G-actin diffusivity $D_{G(c)}$ = 3.0 μm^2/s throughout the volume plus radial advection velocity V_G = 0.90 μm/s in the non-adhesive region. For each simulation, rapid (0.1 s) bleaching was simulated as depicted in **Fig. S1B**, and the recovery of G-actin fluorescence at the center and rear of the bleach zone was quantified and adequately fit to a double-exponential function of time (**Fig. S1C**). Each of these was

then used to define a time-dependent boundary condition $g_{un}(L,t)$ in a 1D simulation, to be compared to the constant-value results at the level of leading-edge recovery (**Fig. S1D**). As expected, the time-dependent boundary condition yields slower recovery, but the $t_{0.5}$ values are only marginally increased (by 42% for DODL and by 25% for diffusion plus advection).

We note that F-actin was not included in these simulations, because accurate calculation of non-diffusive transport requires a prohibitively (in 3D) fine mesh to mitigate the issue of numerical diffusion. This is justified, insofar as G-actin recovery at the rear is concerned; on the timescale of that recovery, the depolymerization of unbleached F-actin near the leading edge is insignificant relative to diffusion of unbleached G-actin from the adjacent cell body.

We further note that we consider the conclusions from the 3D simulations to be conservative, in that the G-actin diffusivity was constant throughout the cell volume. In reality, diffusion within the cell body is expected to be faster than it is in the spillover region, where it is hindered by the excluded volume and tortuosity of the more tightly packed cytoplasm there (in no so small part because of the F-actin concentrated there). Faster diffusion in the cell body would cause faster recovery of $g_{un}(L,t)$ and therefore closer agreement with the leading-edge recovery predicted using the constant-value boundary condition.

4. Exploration of a two-state DODL model of G-actin transport: different diffusivities

Picking up from the end of Section 1 above, if one assumes Fickian diffusion for the cytosolic G-actin species i, we write

$$\mathbf{N}_{G,i} = -D_{Gi}\nabla G_i - \mathbf{V}_{Gi}G_i,$$

where D_{Gi} and $\mathbf{V}_G$ are the diffusivity and anterograde velocity vector of G-actin species i, respectively. Both of these potentially vary with position. Summing the fluxes, we obtain

$$\mathbf{N}_G = -D_G\nabla G - \mathbf{V}_G G;$$
$$\phi_i = \frac{G_i}{G};\quad D_G = \sum_i \phi_i D_{Gi};\quad \mathbf{V}_G = \sum_i (D_{Gi}\nabla\phi_i + \phi_i\mathbf{V}_{Gi}).$$

It is thus shown that there can be a diffusive contribution to the apparent anterograde flow vector (as defined). Considering that

$$\sum_i (\nabla\phi_i) = \nabla\left(\sum_i \phi_i\right) = 0,$$

we conclude that a nonzero contribution requires a substantial disparity in G-actin species i diffusivities and gradients of species i representation ϕ_i. The contribution will be positive/negative if and where the slower/faster diffusers are increasing in

representation as they move towards the leading edge. This suggests that a model considering slower- and faster-diffusing G-actin states might allow steady-state metrics to be achieved, with the faster-diffusing species taking the place of 'advection.' The question is whether or not this will result in slower FRAP, like the scenario of slow diffusion plus true vectorial transport.

To address this possibility, we develop a two-state model, with G-actin species concentrations, G_1 and G_2. They are governed by the steady-state conservation equations,

$$-\frac{dN_{G,1}}{dx} + k_{depol,1}F(x) - r_{12}(x) = 0;$$
$$-\frac{dN_{G,2}}{dx} + k_{depol,2}F(x) + r_{12}(x) = 0,$$

where $r_{12}(x)$ is the (as yet unspecified) net rate of interconversion from species 1 to species 2. To define the boundary conditions at the leading edge, we consider that each of the two species might (or might not) contribute to actin polymerization (through a combination of direct addition or via leading-edge polymerases), with

$$-N_{G,1}(0) = N_{pol,1};\ \ -N_{G,2}(0) = N_{pol,2};$$
$$N_F(0) = N_{pol} = N_{pol,1} + N_{pol,2} = V_F F_0.$$

Some general, steady-state results obtained by combining these equations are:

$$-N_{G,1}(x) = N_{pol,1} - \frac{k_{depol,1}}{k_{depol}} N_{pol}\left[1 - \exp\left(-\frac{k_{depol}}{V_F}x\right)\right] + \int_0^x r_{12}dx$$
$$-N_{G,2}(x) = N_{pol,2} - \frac{k_{depol,2}}{k_{depol}} N_{pol}\left[1 - \exp\left(-\frac{k_{depol}}{V_F}x\right)\right] - \int_0^x r_{12}dx$$

Summing these, we obtain the result from before,

$$-N_{G,1}(x) - N_{G,2}(x) = -N_G(x) = N_{pol}\exp\left(-\frac{k_{depol}}{V_F}x\right).$$

We now consider that only one of the two G-actin species is polymerizable. By inspection of the flux expressions, we see that the flux of the polymerizable form would be assisted by depolymerization directly into that form (or by depolymerization followed by a rapid conversion to that form) and by net conversion from the other, non-polymerizable species. Letting species 2 be the polymerizable form, only for the convenience that $r_{12}(x)$ is positive,

$$-N_{G,1}(x) = \int_0^x r_{12}dx\,;$$
$$-N_{G,2}(x) = N_{pol}\exp\left(-\frac{k_{depol}}{V_F}x\right) - \int_0^x r_{12}dx.$$

If we now assume that transport is by diffusion only, with constant diffusivities, we obtain

$$G_2(x) = G_2(0) + \frac{N_{pol}}{D_{G,2}}\frac{V_F}{k_{depol}}\left[1 - \exp\left(-\frac{k_{depol}}{V_F}x\right)\right] - \frac{D_{G,1}}{D_{G,2}}[G_1(x) - G_1(0)];$$

Given that there is an experimental constraint imposed on the value of $G(L) = G_1(L) + G_2(L)$, we reason that this system only makes sense if the polymerizable species 2 is the slower diffuser; the fast diffusing species 1 shortens the distance species 2 needs to diffuse.

For example, we considered a scenario wherein the species 1 consumption largely occurs close to the leading edge, such that species 1 has nearly constant flux elsewhere. To model this with a minimum number of parameters, we took

$$r_{12}(x) = r_m e^{-ax}(1 - e^{-bx}).$$

Note that the rate vanishes at $x = 0$, considering that we will assume that $G_1(0) \approx 0$ also (consistent with DODL assumptions; note that this also means that the polymerizability of species 1 is moot). The constants a and b are such that both aL and bL are large. Hence, we obtained

$$G_1(x) - G_1(0) = \frac{r_m}{D_{G,1}}\left[\frac{ax - 1 + e^{-ax}}{a^2} - \frac{(a+b)x - 1 + e^{-(a+b)x}}{(a+b)^2}\right],$$

and we used this result to obtain $G_2(x) - G_2(0)$ (with concentrations normalized by F_0). These results are shown in **Fig. S4A**, using parameter values consistent with the simulations presented in main **Fig. 4**: V_F = 0.2 μm/s, L = 10 μm, k_{depol} = 0.01 s^{-1}, $g(0) \approx 0$, and $D_{G,2}$ = 3 μm^2/s (matching our diffusion plus advection scenarios); to this we added $a = b$ = 3 μm^{-1} and $D_{G,1}$ = 12 μm^2/s, and finally r_m = 0.95 s^{-1} was fit to successfully match $g(L)$ = 0.15.

Another way to interpret this model is to set up the overall flux as before, with diffusion only:

$$-N_G(x) = D_{G,1}\frac{dG_1}{dx} + D_{G,2}\frac{dG_2}{dx} = N_{pol}\exp\left(-\frac{k_{depol}}{V_F}x\right),$$

or we can write

$$-N_G(x) = D_{G,2}\frac{dG}{dx} + \left(D_{G,1} - D_{G,2}\right)\frac{dG_1}{dx} = N_{pol}\exp\left(-\frac{k_{depol}}{V_F}x\right).$$

Interpreted this way, one might take the apparent diffusion coefficient as that of the slower, polymerizable species 2, and the second term on the left-hand side as the 'advective' flux:

$$V_G(x)G(x) = \left(D_{G,1} - D_{G,2}\right)\frac{dG_1}{dx}.$$

For the example given above, we calculated the apparent $V_G(x)$ and found that the values were ~ 1 μm/s, consistent with the analysis of the one-species model.

Having shown that a two-state, DODL model can sufficiently match typical experimental constraints at steady state, we turn our attention to the corresponding FRAP predictions, writing unsteady balances for the unbleached species (after bleaching),

$$\frac{\partial G_{un,1}}{\partial t} = D_{G,1}\nabla^2 G_{un,1} - r_{12}(x)\frac{G_{un,1}}{G_1};$$
$$\frac{\partial G_{un,2}}{\partial t} = D_{G,2}\nabla^2 G_{un,2} + k_{depol}F_{un} + r_{12}(x)\frac{G_{un,1}}{G_1}.$$

Applying associated boundary conditions, with the membrane-bound states considered quasi-steady as before, we have

$$N_{Fun}|_{x=0} = V_F F_{un}|_{x=0} = -N_{Gun,2}\Big|_{x=0} = D_{G,2}\frac{\partial G_{un,2}}{\partial x}\Big|_{x=0} = N_{pol}\frac{G_{un,2}}{G_2}\Big|_{x=0};$$
$$-N_{Gun,1}(0) = D_{G,1}\frac{\partial G_{un,1}}{\partial x}\Big|_{x=0} = 0,$$

together with the constant-value boundary conditions at $x = L$. This was applied to our example model of steady-state $r_{12}(x)$ in a 1D bleaching simulation (**Fig. S4B**). The results show that the two-species DODL model and the original DODL model with only one G-actin species yield similar FRAP predictions, unlike those generated when true advection was allowed. This is readily understood when one considers the effects of photobleaching on diffusive transport (explained also in the main-text Discussion): transient, large gradients of unbleached G-actin species yield fluxes that are much greater in magnitude than those associated with the steady state. As demonstrated above, we can construct an 'advective' flux and associated anterograde velocity $V_G(x)$ to achieve a reasonable steady state, but that $V_G(x)$ does not apply to unbleached G-actin in a diffusion-only model. The analogous construct for unbleached G-actin [which we might call $V_{Gun}(x,t)$] is transient and much larger during FRAP.

5. Exploration of a two-state model of G-actin transport: leading-edge polymerizability

We also applied a two-state G-actin transport model to relax the assumption that all of the G-actin at the leading edge is equally polymerizable. Specifically, we addressed whether or not a fairly slow conversion to a polymerizable form might cause slower FRAP with diffusion only. From the previous section, but with constant diffusivity D_G, we have at steady state,

$$D_G \frac{dG_1}{dx} = \int_0^x r_{12} dx\,;$$
$$D_G \frac{dG_2}{dx} = N_{pol} \exp\left(-\frac{k_{depol}}{V_F} x\right) - \int_0^x r_{12} dx.$$

Taking a simple, first-order rate of conversion in this case,

$$r_{12} = k_{12} G_1;$$
$$G_1(x) = G_1(L) \frac{\cosh(x/\lambda_1)}{\cosh(L/\lambda_1)}; \quad \lambda_1 = \sqrt{\frac{D_G}{k_{12}}}.$$

And,

$$G_2(x) = G_2(0) + \frac{N_{pol}}{D_G} \frac{V_F}{k_{depol}} \left[1 - \exp\left(-\frac{k_{depol}}{V_F} x\right)\right] - [G_1(x) - G_1(0)].$$

Obtaining suitable gradients with this model while keeping k_{12} low presents a trade-off. To optimize this, and also so that the flux of polymerizable, unbleached G-actin at the start of FRAP is zero (to give the best chance of slowing FRAP), we constrained

$$G_2(L) = G_2(0) = 0.$$

With this constraint, we set $G_1(L) = 0.15$ and the typical parameter values V_F = 0.2 μm/s, L = 10 μm, and k_{depol} = 0.01 s^{-1}. Hence, we could achieve our objectives for the steady state with assignment of k_{12} = 0.5 s^{-1} and D_G = 15.5 μm^2/s (**Fig. S5A**).

FRAP predictions were executed with the same equations as presented in the previous section; only r_{12} and values of common parameters are different as noted here. While one might think of conversion to the polymerizable state as a 'rate-limiting' step, the results show that FRAP is actually predicted to be comparable to that of the DODL scenario with one, lumped G-actin state (**Fig. S5B**). This is because diffusion and interconversion within the domain occur in parallel, in effect combining to speed up the approach to steady state.

6. Leading-eigenvalue analysis of DODL (constant- and variable-diffusivity) scenarios

The FRAP recovery results for DODL scenarios that might be counterintuitive are:

1) It is perhaps surprising that the recoveries are so fast. The $t_{0.5}$ value for the DODL (constant diffusivity) scenario presented in **Fig. 4** is roughly 1 order of magnitude lower than the characteristic timescale of diffusion, $t_D = L^2/D_{G,DODL(c)}$ = 9.5 s;

2) The variable-diffusivity cases of various forms and diffusivity gradients – subject to the same experimental constraints – yield very similar leading-edge FRAP kinetics.

A physical interpretation of observation 1 (duplicated from the main-text Discussion) considers that, at early times post-bleach, there is a steep, positive gradient of unbleached G-actin and an almost-as-steep, negative gradient of bleached G-actin in the *x*-direction. These sum to maintain the relatively modest, positive gradient of G-actin overall. Therefore, at early times post-bleach, the flux of unbleached G-actin is much greater than at steady state and dominated by diffusion. On a more quantitative level, we note that DODL, with constant G-actin diffusivity and no F-actin depolymerization, has a well-known analytical solution. For such a Dirichlet problem, the leading term of the infinite-series solution decays as $\exp(-t/\tau_1)$, where

$$\tau_1 = \frac{t_D}{\pi^2}$$

(with a time constant 10-fold lower than t_D). Incidentally, the $t_{0.5}$ value for the Dirichlet problem and our values of L = 10 μm and $D_{G,DODL(c)}$ = 10.5 μm^2/s is approximately 1.3 s and scales precisely with t_D. This value is only modestly lower (faster) than the $t_{0.5}$ values of our DODL predictions, which include the depolymerization reaction; in the scenarios considered, F-actin is fully bleached initially, and so this was expected.

To put this on a more formal basis, and to address observation 2 stated above, we cast the DODL problem (with possibly variable diffusivity) as follows.

$$\frac{\partial g_{un}}{\partial t} = \frac{\partial}{\partial x}\left[D_{G,DODL}(x)\frac{\partial g_{un}}{\partial x}\right] + k_{depol} f_{un};$$
$$g_{un}(x,0) = 0;$$
$$g_{un}(0,t) = 0;$$
$$g_{un}(L,t) = g(L).$$

Based on the reasoning above, we neglect the depolymerization term for early times; and, with a standard change of variables, we make the Dirichlet boundary conditions homogeneous:

$$g_{un}(x,t) = b(x) - y(x,t)$$
$$\frac{\partial y}{\partial t} = \frac{\partial}{\partial x}\left[D_{G,DODL}(x)\frac{\partial y}{\partial x}\right];$$
$$\frac{d}{dx}\left[D_{G,DODL}(x)\frac{db}{dx}\right] = 0;$$
$$y(x,0) = b(x);$$
$$y(0,t) = b(0) = 0;$$
$$y(L,t) = b(L) - g(L) = 0;$$

$$b(x) = g(L)\frac{\int_0^x \frac{dx'}{D_{G,DODL}(x')}}{\int_0^L \frac{dx'}{D_{G,DODL}(x')}}.$$

This now conforms to the general problem examined by Farkas and Deconinck (cited in the main text), who showed how to obtain estimates of the eigenvalues for the analogous problem in heat transfer, with variable thermal conductivity. Remarkably, analysis of their work reveals that the leading eigenvalue can be closely approximated by a simple function, such that the leading term of the solution decays with a characteristic diffusion timescale,

$$\tau_1 \approx \left(\frac{1}{\pi}\int_0^L \frac{dx'}{{D_{G,DODL}}^{\frac{1}{2}}(x')}\right)^2 = \left(\frac{L}{\pi}\langle {D_{G,DODL}}^{-\frac{1}{2}}(x)\rangle\right)^2.$$

For constant diffusivity, this matches the well-known result given above.

Given the same experimental inputs, both the constant- and variable-diffusivity DODL scenarios are subject to the same matching constraint, namely

$$V_F \int_0^{x_{match}} \frac{f(x')}{D_{G,DODL}(x')}\,dx' = g(x_{match}).$$

Because the steady-state F-actin profile, $f(x)$, is typically a weak function of x, all plausible $D_{G,DODL}(x)$ at least approximately obey

$$\int_0^L \frac{1}{D_{G,DODL}(x')}\,dx' \approx \frac{L}{D_{G,DODL(c)}}.$$

This explains why all DODL scenarios with sufficiently smooth functions $D_{G,DODL}(x)$ (including constant diffusivity) yield similar FRAP recovery kinetics; they have approximately the same value of

$$\langle {D_{G,DODL}}^{-1}(x)\rangle \approx \left(\langle {D_{G,DODL}}^{-\frac{1}{2}}(x)\rangle\right)^2.$$

SUPPLEMENTAL FIGURES

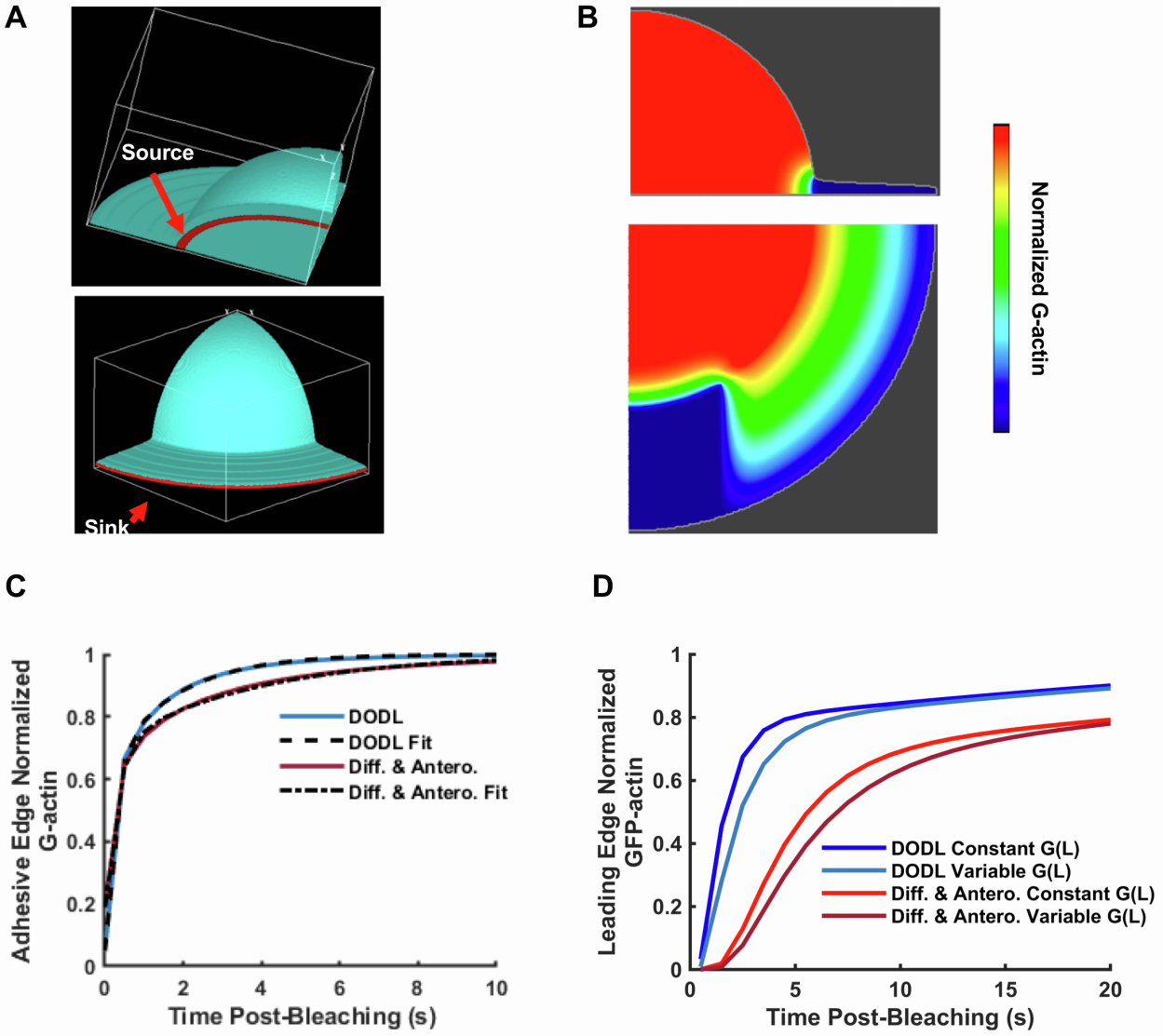

Figure S1. Additional analysis of FRAP model boundary conditions at $x = L$. (A) Reaction-diffusion equations were solved with a 3D geometry similar to those observed experimentally. A steady state G-actin concentration field was established by setting a constant-flux 'source,' localized in a ring pattern at the interface between adhesive and non-adhesive regions (top), and a first-order reaction 'sink' at the most-distal tip of the membrane (bottom). **(B)** G-actin concentration profiles in the YZ (x = 0) and XY (z close to the bottom) planes just after a simulated, 0.1 s bleach event. **(C)** FRAP time courses at the back and center of the bleached area were fit by a double-exponential function. **(D)** These functions were used in place of the constant-value boundary condition in 1D to generate new FRAP predictions.

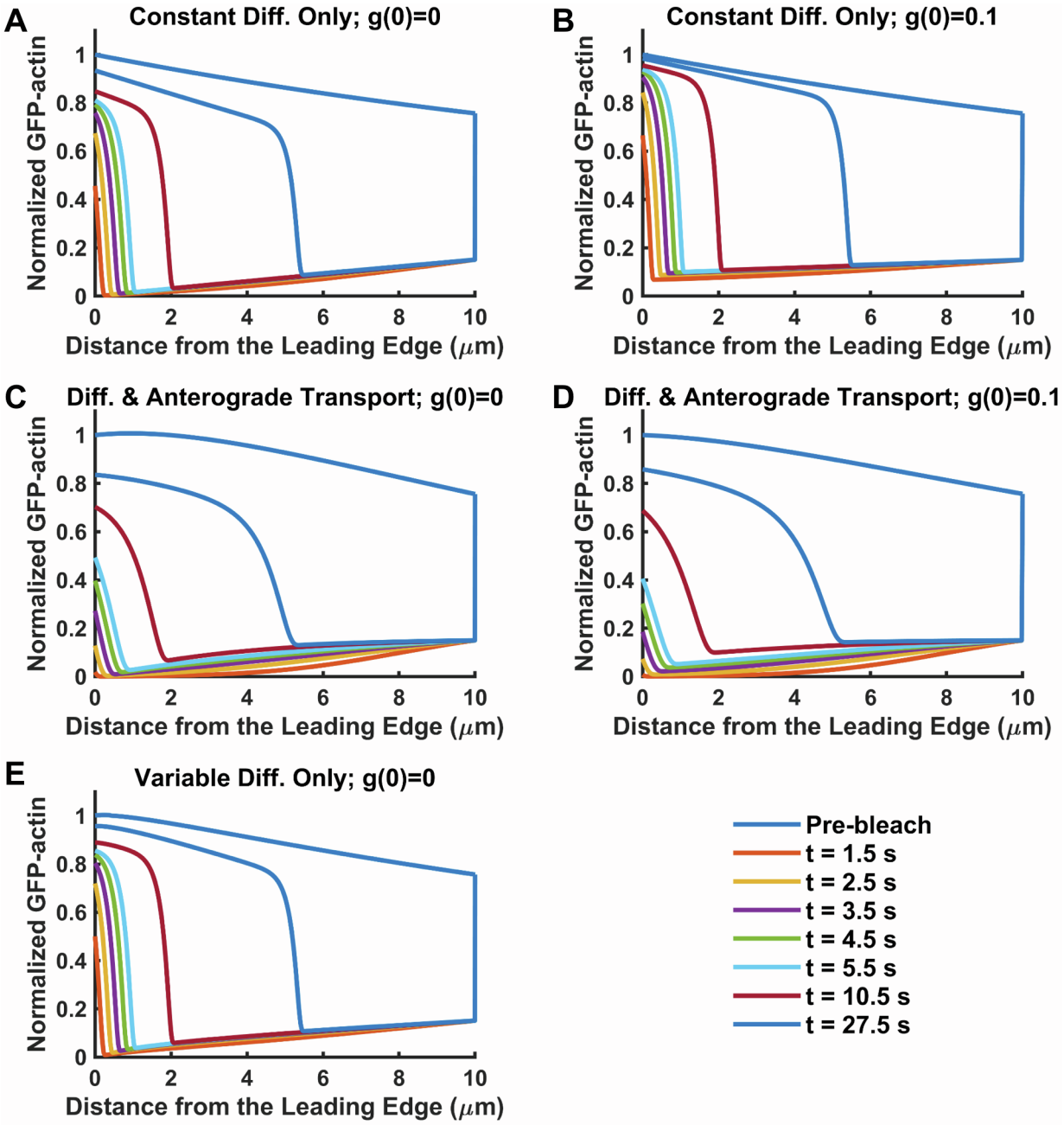

Figure S2. Pre- and post-bleaching line scans of total GFP-actin from 1D simulations. (A) Constant diffusion only (D_G = 10.5 μm^2/s) and $g(0)$ = 0.**(B)** Constant diffusion only (D_G = 29.7 μm^2/s) and $g(0)$ = 0.1. **(C)** Constant diffusion (D_G = 3 μm^2/s) aided by constant anterograde velocity and $g(0)$ = 0. **(D)** Constant diffusion (D_G = 3 μm^2/s) aided by constant anterograde velocity and $g(0)$ = 0.1. **(E)** Variable diffusion only ($D_G(0)$ = 3 μm^2/s).

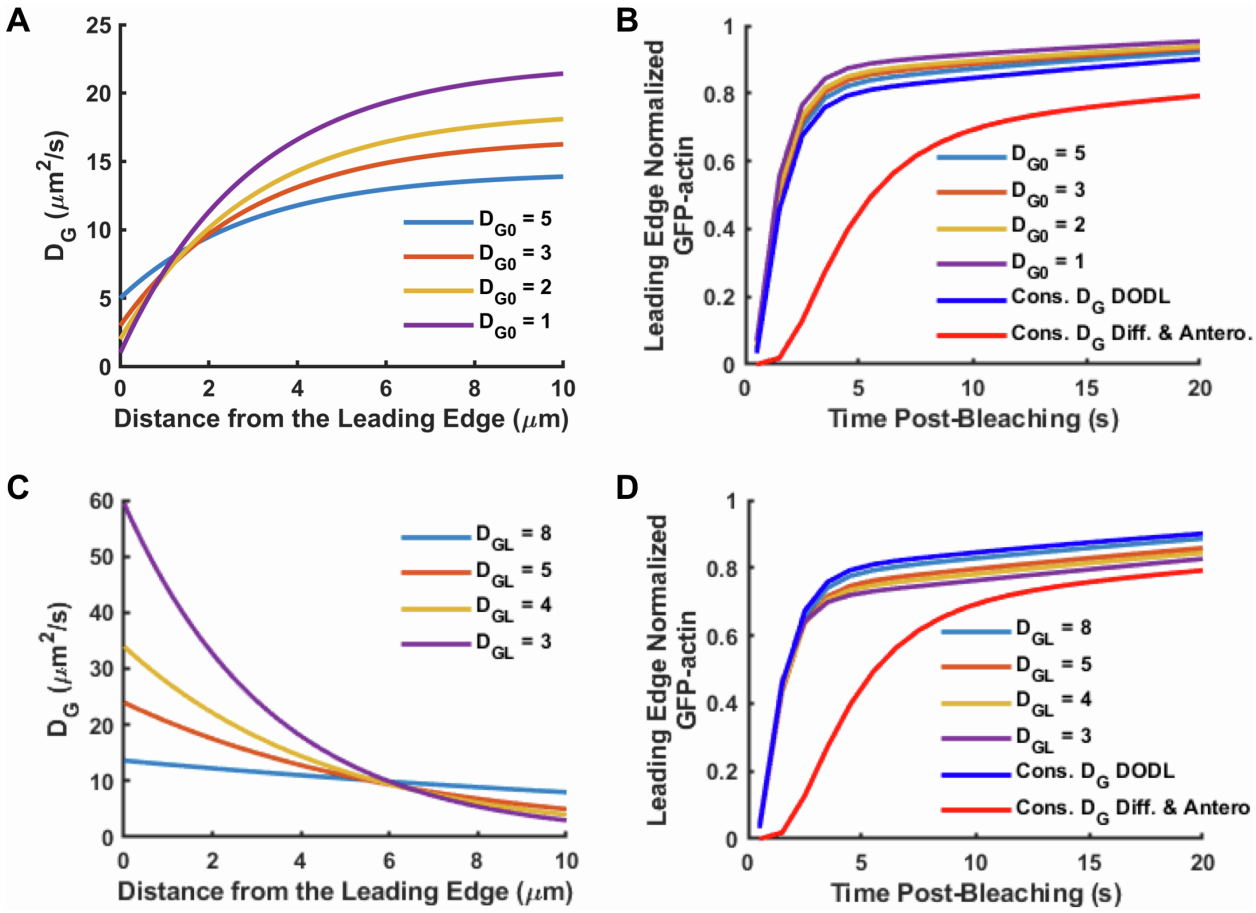

Figure S3. FRAP predictions for DODL scenarios with various $D_{G,DODL}(x)$. Under the same 1D simulation conditions described under **Fig. 4**, we simulated position-dependent G-actin diffusivity profiles that match the leading-edge flux and the G-actin concentrations at both boundaries. **(A)** Increasing diffusivity profiles, with the leading-edge value specified. **(B)** The variable-diffusivity DODL scenarios predict FRAP kinetics similar to the constant-diffusivity DODL scenario, unlike the scenario with $D_{G(c)}$ = 3 μm^2/s and V_G (Antero.) = 0.9 mm/s. **(C&D)** Same as **A**&**B**, respectively, except with decreasing diffusivity profiles and the values at $x = L$ specified.

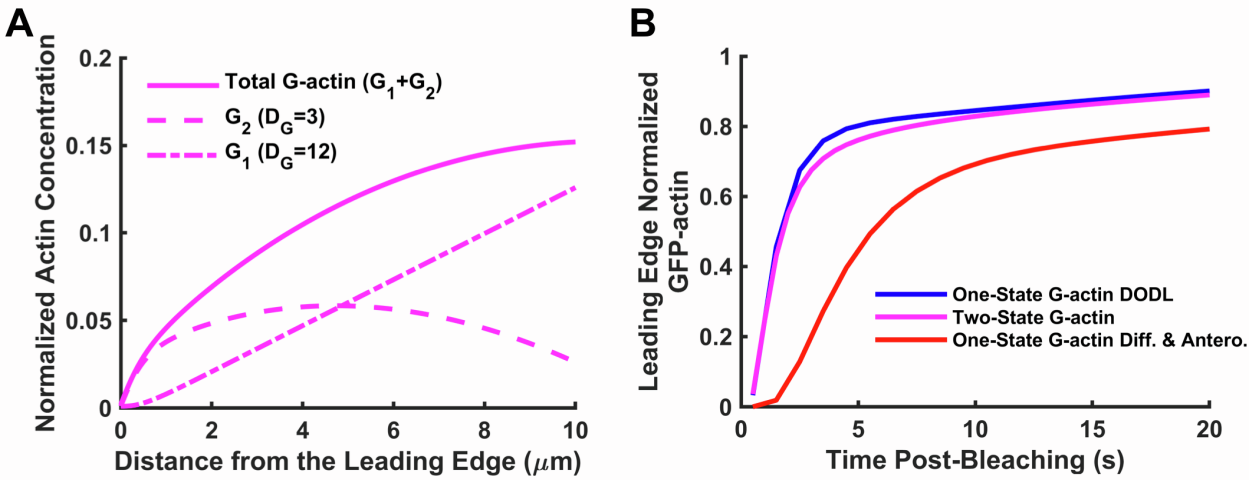

Figure S4. Modeling two states of G-actin with different diffusivities. (A) A slow diffusion of a polymerizable actin pool (G_2) can be offset by conversion from a fast-diffusing pool (G_1) to match steady-state observables. **(B)** The resulting FRAP prediction is nonetheless comparable to that of the 'one-state' DODL scenario, and thus much different from the scenario with constant, slow diffusivity plus anterograde, vectorial transport.

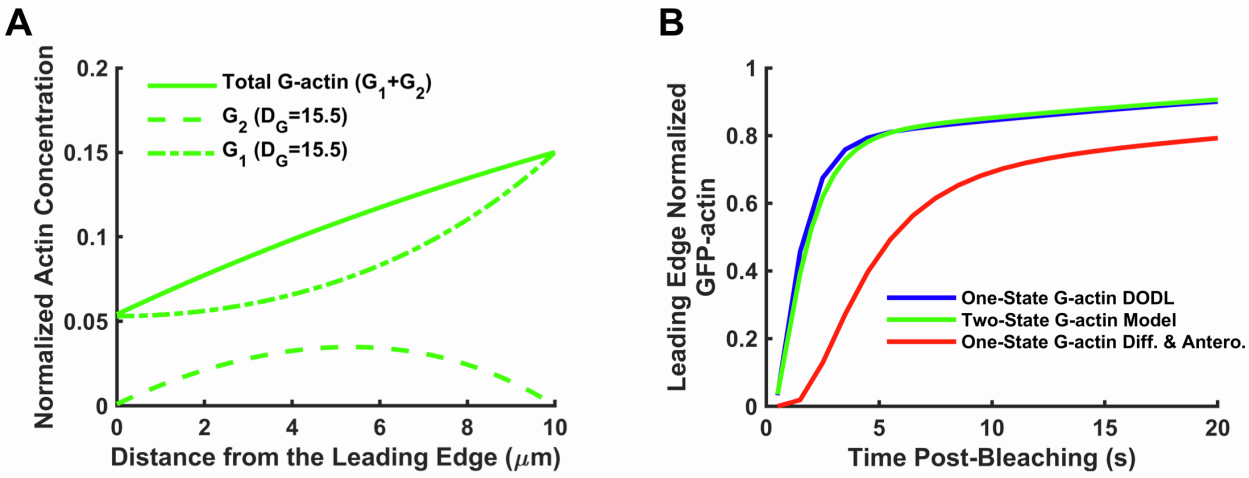

Figure S5. Modeling two states of G-actin with slow conversion to a polymerizable state. (A) With extreme values of parameters, a scenario with slow conversion to a polymerizable state (G_1 → G_2) can match steady-state observables. **(B)** The resulting FRAP prediction is nonetheless comparable to that of the 'one-state' DODL scenario, and thus much different from the scenario with constant, slow diffusivity plus anterograde, vectorial transport.

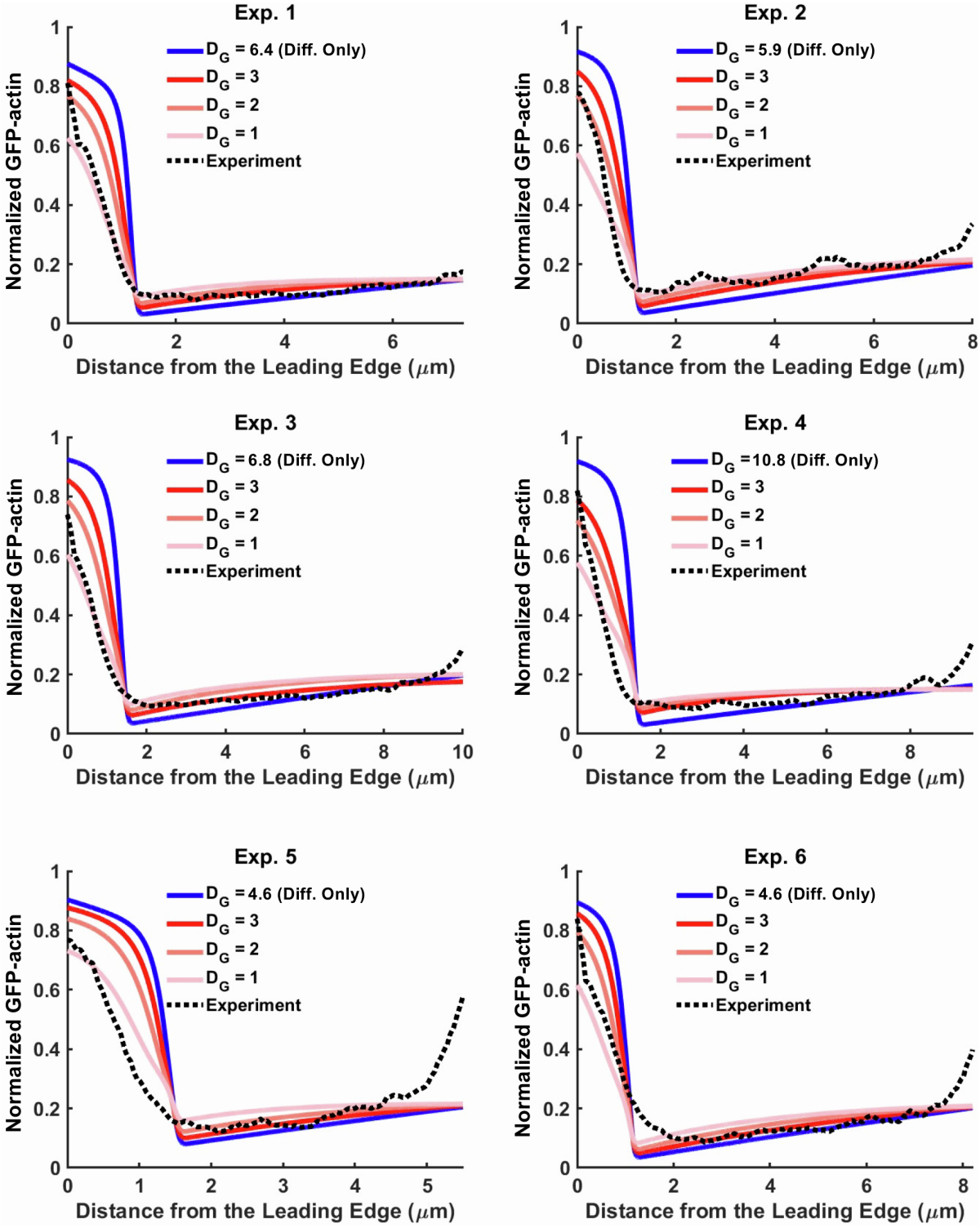

Figure S6. Spatial profiles measured at time = 2*$t_{0.5}$ do not align with the diffusion-only model predictions. Spatial profiles measured at 2*$t_{0.5}$ for six of the seven experiments (the seventh is shown in **Fig. 5C**) in the cohort and their corresponding simulation data for different values of D_G (μm^2/s).

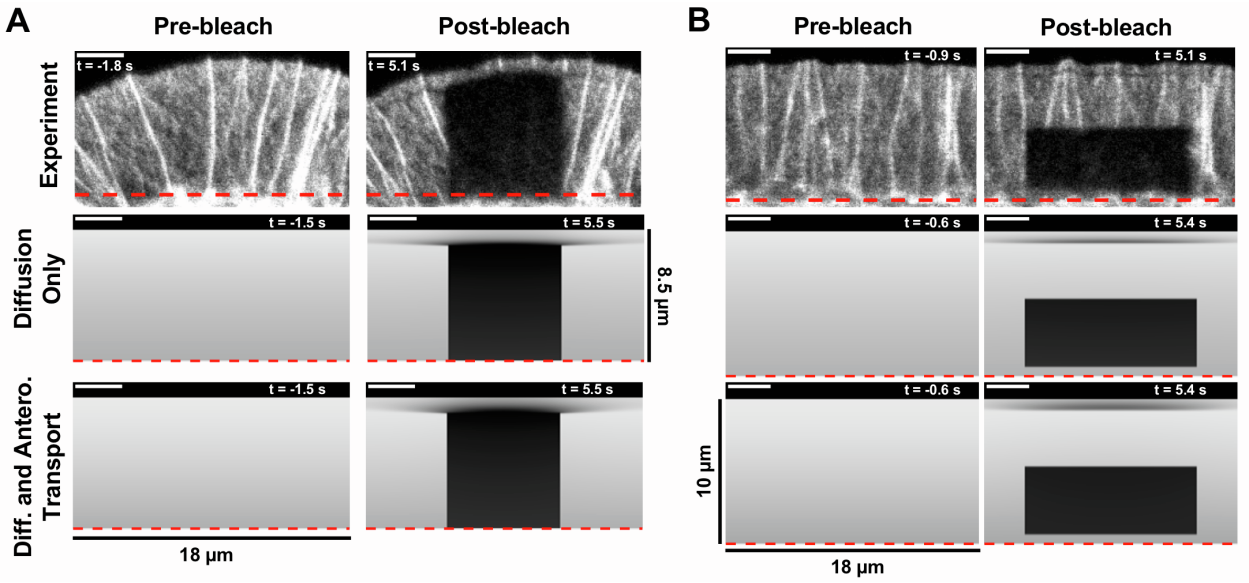

Figure S7. Simulated FRAP scenarios predict the rapid appearance of a thin, dark band, as observed in experiments. Following either full-span **(A)** or partial-span **(B)** bleaching, a thin dark band rapidly appears at the leading edge; because of isotropic G-actin diffusion, the band spreads laterally, outside the width of the bleached area. Model predictions for the key scenarios of DODL and diffusion plus advection (parameterized with $g(0) \approx 0$) are qualitatively consistent with experiments, but in this regard we were not able to discern the quantitative differences between the two scenarios from experiments.

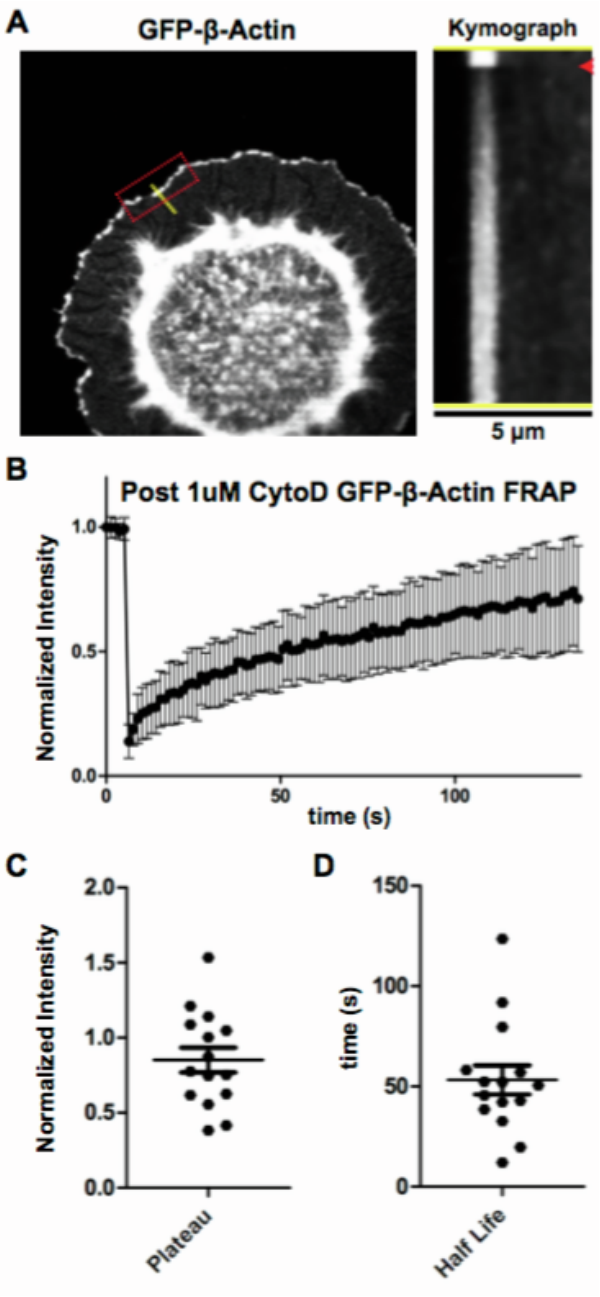

Figure S8. Dynamics of GFP-actin accumulating at spillover protrusion edges following CytoD treatment. (A) The same cell shown in **Fig. 6A**, with a dashed, red box indicating the photobleached region and a yellow line representative of the region from which the adjacent kymograph was generated (duration = 135 s). The red arrow in the kymograph marks when the bleach occurred. **(B)** FRAP recovery curves averaged across 15 cells bleached and monitored as depicted in **A**. Error bars represent the Standard Deviation of the Mean. **(C&D)** Plots of the plateau value (**C**) and half-life (**D**) of a one-phase exponential curve fitted to the FRAP curve of each cell included in the analysis shown in **B**.

CAPTIONS FOR SUPPLEMENTAL MOVIES

Movie S1. Supplemental movie for Figure 2A. Spillover protrusion labeled with GFP-actin bleached at a discrete region between the leading edge and the fibronectin attachment zone. Scale bar = 5 μm, and time stamp is in MM:SS format

Movie S2. Supplemental movie for Figure 2A. Spillover protrusion labeled with GFP-actin bleached in a wide stripe running all the way from the leading edge to the fibronectin attachment zone. Scale bar = 5 μm, and time stamp is in MM:SS format.

Movie S3. Supplemental movie for Figure 2C. JR20 Fibroblast expressing GFP-actin plated on a triangle micropatterned Fn island and bleached all throughout the spillover protrusion zone. Scale bar = 10 μm, and time stamp is in MM:SS format.

Movie S4. Supplemental movie for Figure 2C. JR20 Fibroblast expressing GFP-actin plated on a square micropatterned Fn island and bleached all throughout the cell body at and above the Fn attachment site. Scale bar = 10 μm, and time stamp is in MM:SS format.

Movie S5. Supplemental movie for Figure 6A. JR20 Fibroblast expressing GFP-actin plated on a circle micropatterned Fn island and treated with 1 μM between frames marked with 00:36 and 00:37. Scale = 10 μm and time stamp is in MM:SS format (there was a ~15-20s pause between 00:36 and 00:37 for drug wash in, which is not shown/accounted for in the time stamp).